POLITECNICO
MILANO 1863

SCUOLA DI INGEGNERIA INDUSTRIALE
E DELL'INFORMAZIONE

Variable Impedance Control of a Surgical Robot for Spinal Surgery

Tesi di Laurea Magistrale in
Automation and Control Engineering - Ingegneria dell'Automazione

Author: **Riccardo Monaco**

Student ID: 969134
Advisor: Prof. Elena De Momi
Co-advisors: Elisa Iovene
Academic Year: 2021-22

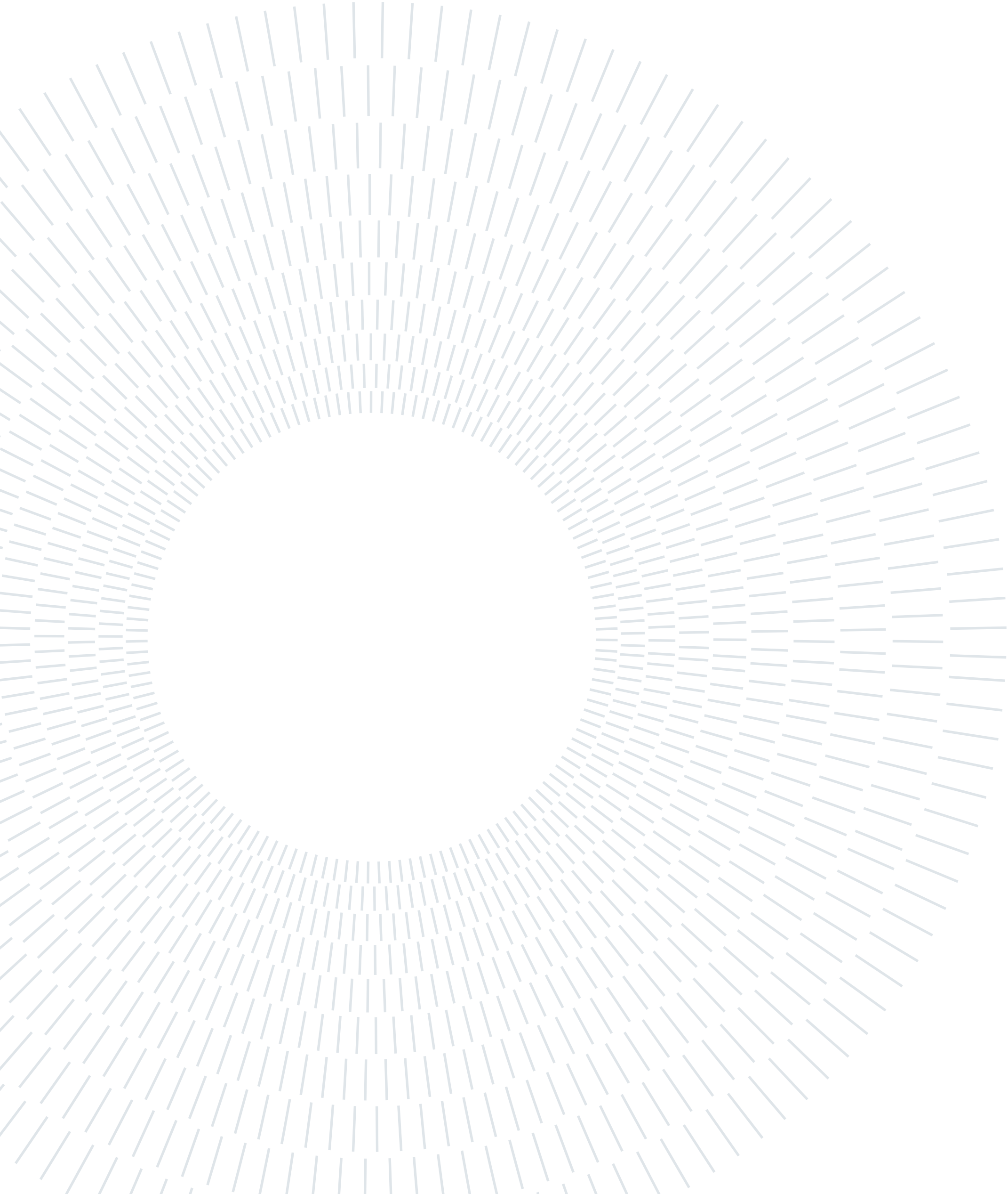

Abstract

Over the last decades, research has been focused on introducing robotic systems in surgical operations. This is supported by the idea that such systems can bring great advantages to both the patient and the surgeon, improving the accuracy and safety of the procedure. The use of robotic systems in spinal surgery is currently limited to a few procedures, such as pedicle screw placement. This is mainly due to the complexity of the spine structure which poses significant challenges in surgical operations, requiring a high level of precision from the surgeon and carrying a significant risk of injury to the patient. The objective of this work was to introduce a robotic manipulator that can assist surgeons in performing vertebral osteotomy procedures, a type of spinal surgery that involves the removal of a section of the vertebral bone while ensuring the preservation of delicate surrounding tissues such as the spinal cord, nerve root, and blood vessels. The proposed approach involved a variable impedance control scheme within a shared-control framework. This enabled the surgeon to manually guide the robot, whose stiffness was adjusted in real-time based on two control laws that considered the human intention, as extracted from the EMG signal, and the contact force measured during the procedure. The control laws enabled the robot to exhibit compliant behavior when in contact with bone-like material, and increased stiffness parameters when in contact with critical tissues. The system was validated by means of a user study in order to test the research hypothesis, i.e. the introduction of a variable impedance control law could prevent users from damaging delicate structures while allowing them to operate on a bone-like material. The proposed approach was compared with a constant parameter impedance control, and the task was performed on different materials with varying mechanical properties. The results indicated that the system successfully reduced contact force and in-contact displacement when in contact with delicate materials, demonstrating its ability to avoid damaging delicate structures. Furthermore, a subjective survey showed that the proposed approach successfully prevented movement when needed, as users felt unable to complete the task.

Keywords: Spinal surgery, variable impedance control, EMG

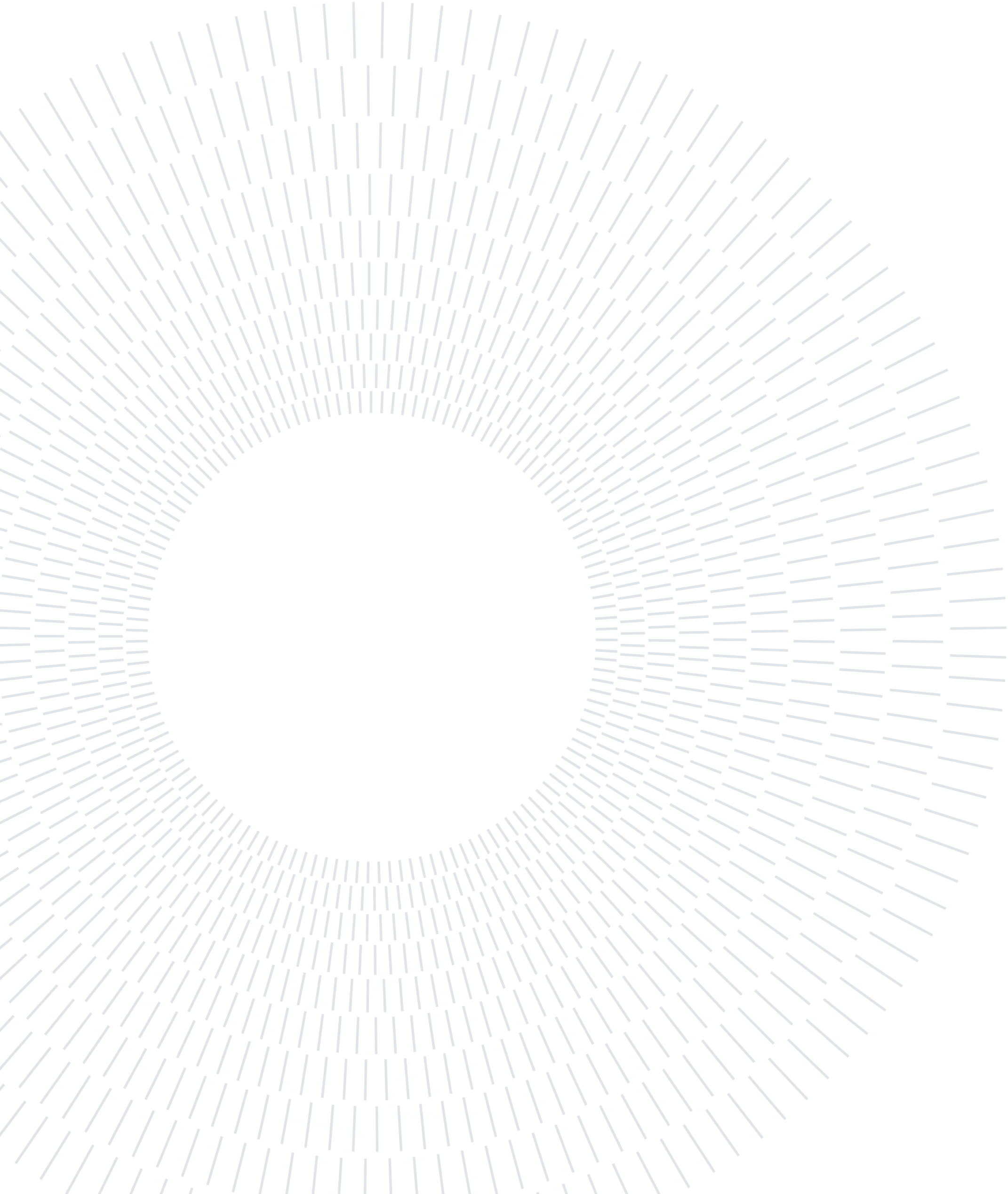

Abstract in lingua italiana

Negli ultimi anni, numerose ricerche sono state svolte nell'ambito della chirurgia robotica, con lo scopo di introdurre dei sistemi robotici a supporto del chirurgo. Questo è supportato dall'idea che tali sistemi possano portare grandi vantaggi sia al paziente che al chirurgo, migliorando la precisione e la sicurezza della procedura. L'uso di sistemi robotici in chirurgia spinale è attualmente limitato a poche procedure, come il posizionamento delle viti peduncolari. Questo è principalmente dovuto alla complessità della struttura spinale, che rende le operazioni chirurgiche particolarmente difficili, richiedendo un elevato livello di precisione da parte del chirurgo e comportando un significativo rischio di lesioni per il paziente. L'obiettivo di questo lavoro è stato quello di introdurre un manipolatore robotico in grado di assistere i chirurghi nell'esecuzione di procedure di osteotomia vertebrale, un tipo di intervento di chirurgia spinale che comporta la rimozione di una sezione dell'osso vertebrale, garantendo la conservazione dei tessuti circostanti più delicati, come il midollo spinale, tessuti nervosi e i vasi sanguigni. L'approccio proposto ha previsto uno schema di controllo ad impedenza variabile, in un framework di controllo condiviso tra robot e chirurgo. Ciò ha permesso al chirurgo di guidare manualmente il robot, la cui rigidità è stata regolata in tempo reale in base a due leggi di controllo, che tenevano conto dell'intenzione umana, estratta dal segnale EMG, e della forza di contatto misurata durante la procedura. Le leggi di controllo hanno permesso al robot di mostrare un comportamento flessibile quando era a contatto con materiale simile all'osso e di aumentare i parametri di rigidità quando era a contatto con tessuti critici. Il sistema è stato validato mediante uno studio sperimentale per testare l'ipotesi di ricerca, ovvero che l'introduzione di una legge di controllo ad impedenza variabile potesse prevenire gli utenti dal danneggiare le strutture delicate consentendo loro di operare su un materiale simile all'osso. L'approccio proposto è stato confrontato con un controllo ad impedenza a parametro costante e il compito è stato eseguito su diversi materiali con proprietà meccaniche variabili. I risultati hanno indicato che il sistema ha ridotto con successo la forza di contatto e lo spostamento durante il contatto con i materiali più delicati, dimostrando la sua capacità di evitare danni a tali strutture. Inoltre, un sondaggio soggettivo ha mostrato che l'approccio proposto ha impedito con successo il movimento quando necessario, in quanto gli utenti si sono sentiti incapaci di completare il compito.

Parole chiave: Chirurgia spinale, controllo d’impedenza variabile, EMG

Contents

Abstract **i**

Abstract in lingua italiana **iii**

Contents **v**

Introduction **1**

1 Literature review **5**
- 1.1 Robotic systems in spinal surgery 5
- 1.2 Hands-on control in surgical robots 6
- 1.3 EMG Human force estimation 9

2 Medical scenario **13**
- 2.1 Mechanical characterization 15

3 Materials and methods **17**
- 3.1 KUKA LWR IV+ 17
  - 3.1.1 Kinematics 19
  - 3.1.2 Dynamic model 21
  - 3.1.3 Fast Research Interface 22
- 3.2 Sensors 26
  - 3.2.1 Force Sensor 26
  - 3.2.2 Emg sensor: MyoWristband 29
- 3.3 Control Strategy 33
  - 3.3.1 Theory and modeling of impedance control 33
  - 3.3.2 Proposed control strategy 35
  - 3.3.3 Passivity analysis 40
- 3.4 Experimental setup 46
  - 3.4.1 System validation 46

3.4.2 User Study 47
3.4.3 Choice of control parameters 50

4 Results 53
4.1 Force sensor 53
4.2 Human force estimation 54
4.3 Validation of control scheme 55
4.4 User study 57

5 Conclusions and future developments 63

Bibliography 65

List of Figures 69

List of Tables 73

Acknowledgements 75

Introduction

Vertebral osteotomy is one of the most common operations in spine surgery and it is a procedure that involves removing a portion of the vertebra to correct spinal deformities[1], such as kyphosis or lordosis (Figure 1).

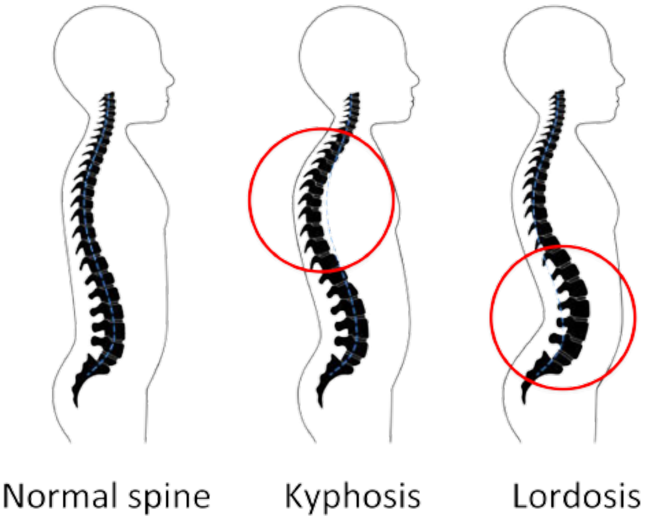

Figure 1: Examples of spinal deformities. Kyphosis: excessive curvature in the upper spine section. Lordosis: excessive curvature in the lower spine section

While vertebral osteotomy can be highly effective, it is a complex and delicate procedure that requires a high degree of precision and skill from the surgeon. The difficulty and duration of the operation can vary significantly depending on the classification of the spinal osteotomy. Nowadays, the operation is performed manually by the surgeon, who makes an incision on the back of the patient to access the affected vertebrae and uses various surgical tools, including drills, saws, or an osteotome (Figure 2), to remove a portion of the vertebra. After the bone removal, the remaining portions of the vertebra are repositioned and stabilized using screws, rods, or other spinal instrumentation. However, this approach carries significant risks of nerve damage, spinal cord injury, bleeding, infection, and other complications. For these reasons, in recent years, numerous support tools and techniques, such as image guidance, pre-operative planning with 3D models, and robotic systems, have been developed.

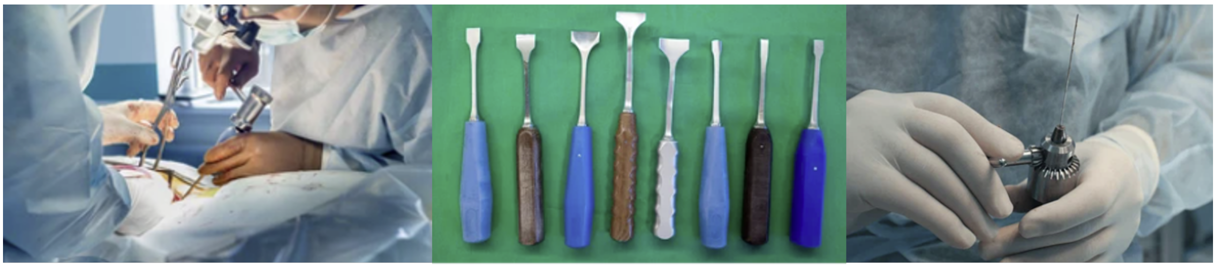

Figure 2: On the left, a surgeon is depicted while using a small hammer and an osteotome (or chisel). In the middle, different types of osteotome are shown. On the right, a surgeon is holding a bone drill.

Over the last decades, many robotic systems have been successfully integrated into surgical operations. The advantages offered by medical robots may be grouped into three areas[2]. The first is the potential to significantly enhance surgeons' technical capability in performing procedures. While humans possess hand-eye coordination and can adapt to various scenarios, they are susceptible to fatigue and distractions, which may lead to errors. The movement of human hands may suffer from poor and limited accuracy in following a trajectory, due to their susceptibility to tremors. In contrast, robotic systems are not subjected to fatigue and provide a high level of geometric accuracy, as the position and orientation can be controlled to follow and match a particular pattern or trajectory. Secondly, medical robots have the potential to prevent surgical instruments from unintentionally harming delicate structures, thanks to the use of active constraints like no-fly zones or virtual fixtures. This lead to better surgical outcomes reduced surgery duration, and less mental workload for the surgeon [3]. Finally, medical robots offer the ability to maintain consistency during procedures and gather detailed online information about the performance, using for example robot sensors and cameras. This information can be saved and analyzed to to develop better surgical plans by examining multiple cases or to monitor patient progress.

Human-Robot Interaction (HRI), in particular, is rapidly evolving and has the potential to transform healthcare practices [4], but its use in the field of neurosurgery is still limited. This is due to the critical nature of surgical interventions that involve neurological and vascular structures, such as those in the brain or spinal cord, which require high precision and accuracy. While HRI can improve surgical outcomes by enhancing precision and reducing the risk of human error, its use is limited to procedures where the benefits outweigh the risks [5], and where the surgeon's skills and experience can be effectively leveraged. As a result, HRI is currently limited to a few specific procedures. For instance, in brain surgeries, HRI is involved in biopsy targeting, electrode placement[6], and laser ablative procedures[7]. Similarly, progress made in surgical techniques and technology for spinal interventions has led to the development of robots that can successfully assist with pedicle screw placement[8].

It is important to highlight that the goal of using robotic-assisted spine surgery is not to replace the surgeon but rather to enhance their capacity to provide high-quality patient care. Moreover, there is a growing interest in exploring the use of HRI for more complicated spinal procedures, such as vertebral osteotomies and tumor resections. These procedures require a high degree of precision and accuracy, as well as a thorough understanding of the complex anatomy of the spine. By leveraging the advanced sensing and control capabilities of robotic systems, HRI has the potential to improve surgical outcomes by providing surgeons with advanced tools to enhance their precision and dexterity. However, before HRI can be widely adopted for more complex procedures, several technical and clinical challenges must be overcome. These challenges include developing more advanced robotic control strategies and ensuring the safety and efficacy of these systems through rigorous validation in clinical trials. Addressing these challenges is crucial to unlocking the full potential of HRI in the field of neurosurgery and other medical specialties.

The aim of this work is to develop a control strategy for robotic systems in hands-on vertebral osteotomy procedures. In this scenario, the robot is equipped with the surgical tool on the end effector, is not fully autonomous, and provides support to the surgeon, who manually guides the robot with direct contact. For this reason, an adaptive impedance control strategy was developed, such that, measuring the contact force between the end effector and the material, and the human force exerted on the robot, the robot's compliantness could be changed accordingly. In particular, when the robot was in contact with critical tissues, the rigidity of the robot increased, and a position signal proportional to the contact force was generated to reduce the risk of damaging such tissues. The contact force was measured using a force sensor mounted on the end effector, while the human force was estimated starting from electromyographic (EMG) signals. To ensure the stability of the system, a passivity filter was used to regulate the variations of the impedance parameters. The ultimate goal of this study was to provide a control strategy that could improve the safety of the operation while reducing the mental workload of the surgeon.

.

The thesis is structured as follows:

- Chapter I: "Literature Review". It presents an overview of the present-day advancements in robotic systems used in spinal surgery, with a particular emphasis on hands-on robotic-assisted procedures. Additionally, the chapter covers the latest advancements in estimating human force using EMG signals.
- Chapter II: "Medical Scenario". In this chapter, the medical scenario is discussed. A general overview of the structure of a vertebra is provided, followed by a detailed description of the osteotomy procedure.
- Chapter III: "Materials and Methods". It presents an overview of all the components used in the study, including the hardware and control strategy. The Kuka-LWR4+ architecture, as well as the force and EMG sensors, are discussed in detail. A detailed description of the control law is reported, together with the stability and passivity proof. Finally, the experimental setup is discussed.
- Chapter IV: "Results". The results of the performed experiments are reported and further discussed in this chapter.
- Chapter V: "Conclusions and Future Developments". The chapter reports the final conclusions of this study, along with future possible developments.

1 | Literature review

In this chapter, we take a closer look at the advancements in robotic technology for spinal surgery, followed by a detailed examination of hands-on control robotic frameworks in the second section. The third section focuses on the current state of the art in human force estimation from electromyographic (EMG) signals.

1.1. Robotic systems in spinal surgery

Research in the field of robotics in spine surgery is motivated by the idea that robotic systems can bring numerous advantages for both surgeons and patients. Robotic technology has the potential to improve safety, accuracy, and efficiency in medical procedures. The area of focus in this field is robotic-assisted spinal instrumentation, with a particular emphasis on pedicle screw placement operations, illustrated in Figure 1.1. Current technologies include the ExcelsiusGPS (Globus Medical, Audubon, PA, USA), Mazor X Stealth Edition (Medtronic, Dublin, Ireland), and the ROSA ONE Spine (Zimmer Biomet, Warsaw, IN, USA) [9].

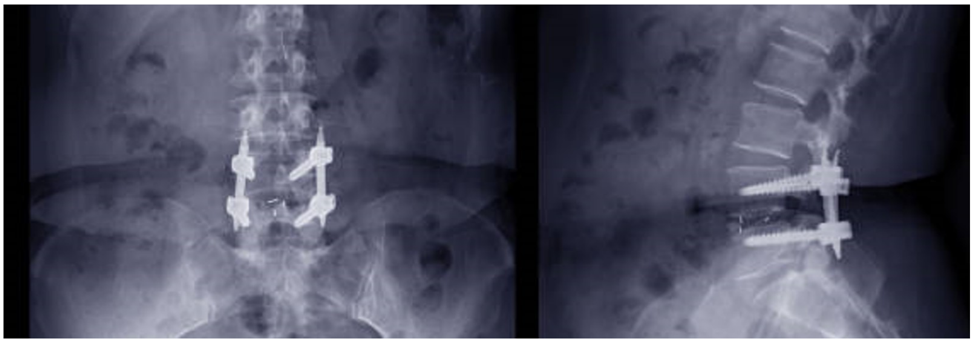

Figure 1.1: Pedicle screw operation outcome: screws are placed inside a vertebra to stabilize the spine. Left: front view. Right: side view.

Several approaches have been studied for pedicle screw placement. A systematic review of clinical studies was conducted by [10], covering the period from January 2000 to August 2021. The study compared traditional techniques with modern techniques, including robotic assistance, and found out that robot-assisted placement resulted in the highest level of optimal screw placement and the lowest incidence of complications. On the other hand, freehand placement had a higher incidence of complications and a greater margin of error in screw misplacement.

The study described in [11] uses the Mazor X Stealth Edition Robotic Guidance System (Figure 1.2). This system enables the surgeon to manually perform drilling and screw insertion while the robotic arm changes its position and orientation to provide a pre-planned screw trajectory and entry point. It is discussed that, compared to conventional techniques, robotic-guided pedicle screw placement offers several benefits, including improved accuracy and safety in screw insertion, precise planned screw positioning, reduced radiation exposure for the surgeon and patient, and decreased operating time. Moreover, no intraoperative complications related to the placement of the pedicle screws or the use of the robot were observed.

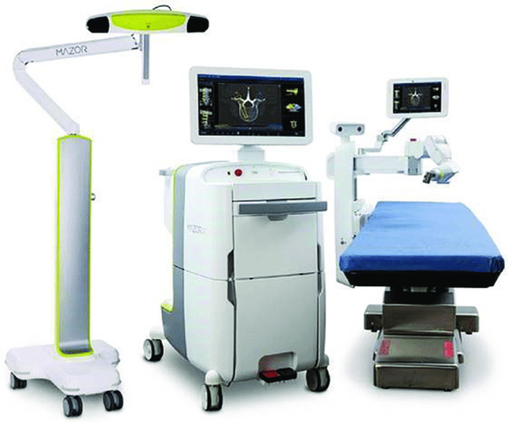

Figure 1.2: Mazor X stealth edition platform. Navigation tracking camera (left), the base station (middle), bed-mounted robotic arm with end effector (right)[12]

1.2. Hands-on control in surgical robots

Regarding HRI and more precisely hands-on control, impedance or admittance Control is the most commonly used strategy for controlling robots [13]. The aim of this framework is to regulate the robot-environment interaction by exploiting the robot's impedance characteristics, such as stiffness, damping, and inertia. By modifying these parameters, the robot can react to external forces in a manner that suits the specific task. In the past three decades, numerous studies have been conducted to adjust the robot's impedance both for robot-environment and human-robot interaction. Some of these studies have used impedance/admittance models with fixed parameters, while others have focused on time-varying, state-dependent impedance control, and real-time online learning of impedance parameters for different HRI applications. In [14], a constant impedance controller is developed for robotic-assisted needle operations. Using a fiber optic force sensor integrated into the needle tip, the interaction force is used to recognize the different tissues, and the impedance controller allows the robot to adjust its behavior. Experiments were performed on layered pig tissue with an automatic robotic needle system, and the study proved that the control strategy is effective to avoid excessive insertion force during the procedure, reducing the risks.

There are various types of impedance control including velocity-based, force-based, and EMG-based. All these methods, if required, allow to modulate dynamically of the robot's impedance parameters and tuning in real-time, based on the collaborative task objective and the human's physical behavior, aiming to improve the robot's compliance and/or stability during interaction with the human and the environment. Velocity-based impedance control focuses on precise task performance by using high impedance to emulate subtle movements at low velocities. Conversely, the low impedance is used for performing large movements at high velocities: depending on the task at hand and the required velocity, impedance parameters can be set to obtain the desired performances. A similar approach is used in [15], in which a variable damping controller is developed in order to help the surgeon reach the surgical working area. In particular, given a visible surgical target, the damping parameter is changed as the user guides the robot toward the target. The strategy is compared to gravity compensation control and constant damping control, showing higher pointing accuracy and intuitive convergence to the target, while reducing the user effort.

Force-based impedance control is crucial for controlling the interaction force between the robot and the environment. This type of control is particularly important in tasks that require a certain level of force, such as industrial applications or to impose a direct HRI force control[16]. The study proposed in [17] presents a force-based approach to achieve compliant behavior of the end effector during micro-suturing procedures. The study uses a variable control framework that successfully achieved co-manipulation accuracy or compliance based on the intended motion of the human, measured using a 6-DOF force sensor. In [18], a Remote Center of Motion (RCM) is imposed to guarantee the stability of the robot's motion. In Robotic-Assisted Minimally Invasive Surgery the surgeons performes small incisions in the patient's body to insert the trocar, a thin, elongated medical device, into the patient's internal organs, which is then manipulated by the surgeon. To avoid complications, the incision walls should not be subjected to lateral forces. For this reason, the incision is imposed as RCM and to yield this constraint a target admittance model is designed in joint space, which means that given as input the measurement of the human force, joint position, and velocity references are generated accordingly. In particular, the admittance model decouples the free motion and the RCM constraint motion, so that the RCM constraint is not affected by human forces and that passivity is guaranteed. Results successfully indicate a trocar displacement of less than 1 mm.

In HRI, communication between the user and the robotic system is key. In particular, the robot needs to perceive and elaborate on the operator's activities during the task, in order to provide actual support. Human activity is usually represented by the force applied, which can be directly measured with force sensors, or estimated starting from EMG signals. In EMG-based impedance control, the stiffness of the robot is adjusted in real-time by analyzing EMG signals from the user's muscles, which estimate the human arm's stiffness or force. In [19], an electromyography-based strategy is proposed to distinguish between operator forces and those resulting from interactions with the environment. To estimate human force, data collection was performed by placing 8 EMG sensors on the user's shoulder, chest, and arm. The robot's stiffness and damping are adjusted based on both the contact force and the estimated human force. In addition to that, a passivity filter is developed, and further explored in [20], to ensure system stability. Experiments illustrated the advantages of this strategy when humans, robots, and the environment interacted with each other. In [21], a sensor-free framework for robot-assisted arthroscopy surgery is developed. In this procedure, the robot helps increase surgical accuracy and precision, while providing physical support for holding the tool when the surgeon is not using it, through impedance control. The study shows that the system is able to obtain compliant behavior during physical HRI.

To enhance safety during surgery, robotic systems can provide constraints tailored to specific operating regions. In [22], a control scheme based on dynamic active constraints intended for hands-on robotic surgery was developed. This methodology used a computer vision technique to produce a smooth and continuous function, which surrounded the points of the surface to be constrained. In order to control the robot to lie on the zero sets of this constraint function, a dynamic controller was derived and incorporated with an impedance controller. The feasibility of the approach was demonstrated both in simulation and with a Kuka LWR-IV+. In [23], a hands-on robot-assisted framework is designed for mandibular angle split osteotomy. This framework measures the surgeon's applied force and divides the surgical areas into three categories based on tool accessibility: allowed, marginal, and forbidden areas. A *tanh* function is used to adjust the admittance behavior during human-robot interaction. The Virtual Fixtures-based policy prevents sudden changes in motion, thereby improving safety performance.

1.3. EMG Human force estimation

An EMG signal captures the electrical signals generated by muscle contractions, which are controlled by the nervous system and can be measured through an electromyograph. EMG has numerous clinical and biomedical applications and serves as a fundamental tool in comprehending the behavior of the human body under both normal and pathological conditions (Figure 1.3).

Figure 1.3: Examples of EMG usage in modern medicine. Electrodes are placed on patients' muscles to measure their activity. Patients are asked to contract or tighten the involved muscles, i.e. closing the hand or bending the leg.

The muscle activation recorded in EMG signal can be used for various applications, ranging from enhancing gesture recognition to controlling robotic arm-hand systems. Considering the latter, in [24] a multiclass classification was performed to characterize different muscular co-activation patterns for reach-to-grasp movements. In particular, six different classification techniques were used, with Random Forest being the most successful one. In [25], MyoWristBand was used to get electromyography from the user's arm, train a model for hand gesture recognition for prosthetic arms.

There are several methods for estimating the force starting from EMG signals, including model regressions, machine learning techniques, and neural networks. Linear regression models can be used to estimate the force by determining the slope and intercept of the linear correlation between the EMG signal and the force [26]. The model can be expressed as:

$$\boldsymbol{F_m} = \beta_0 + \beta_1 \boldsymbol{EMG} \tag{1.1}$$

where $\boldsymbol{F_m}$ is the force generated by the muscle, $\boldsymbol{EMG}$ is the EMG signal, β_0 is the intercept, and β_1 is the slope of the linear relationship. In general, linear regression models have limitations given the fact that the relationship between the EMG signal and the force generated by the muscle can be non-linear. For this reason, using non-linear models, such as polynomial, exponential, or sigmoidal regression techniques, can be more useful in certain applications. As reported in [27], a high number of non-linear mathematical models were proposed in the literature, in the past years. In the study, a convex form of an exponential EMG-to-force model is proposed, and each muscle's coefficient is estimated using Least Squared method. A statistical comparison between other estimation methods like Regularized Least Squares, Support Vector Machines, and Artificial Neural Networks shows that this technique gives better outcomes, even though it presents several limitations, such as using a specific force trajectory for training, that could provide information about muscle excitation, instead of a random force trajectory. In recent years, Neural Networks and Machine Learning algorithms became a popular technique that can be used for force estimation (Figure 1.4).

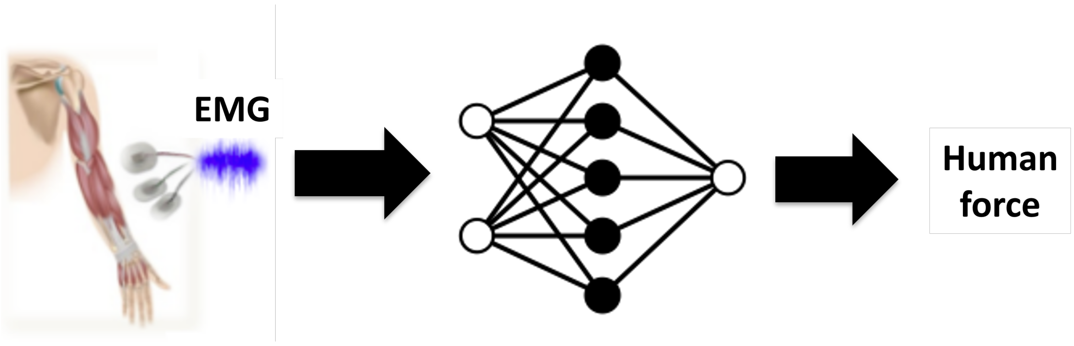

Figure 1.4: Artificial neural networks can be used to estimate muscle forces from EMG measurements

In [28], a convolutional neural network was implemented to provide a way of estimating the interaction force between humans and robots in HRI frameworks, without using prior knowledge of the arm biomechanical model. The proposed methods were compared with other approaches, such as artificial neural networks and long short-term memory (LSTM), showing a lower force error for the designed regression, guaranteeing a higher prediction accuracy. In [29], the problem of force estimation starting from surface electromyography signal was discussed. In particular, the signal was collected from an armband-like device and the work investigated the problem of channel selections. The study proved that six channels are enough to provide an accurate force estimation, because, using a recurrent neural network, the temporal relation between EMG and output force can be successfully captured. In [30], considering an HRI framework, a deep neural prediction network using a one-dimensional convolutional structure was proposed to learn the EMG features from three-channel EMG signals. An estimate of the gripping force is obtained and compared to the one obtained with a two-dimensional convolutional neural network method and a feature-based linear regression, showing better prediction outcomes, in terms of R^2 and MSE.

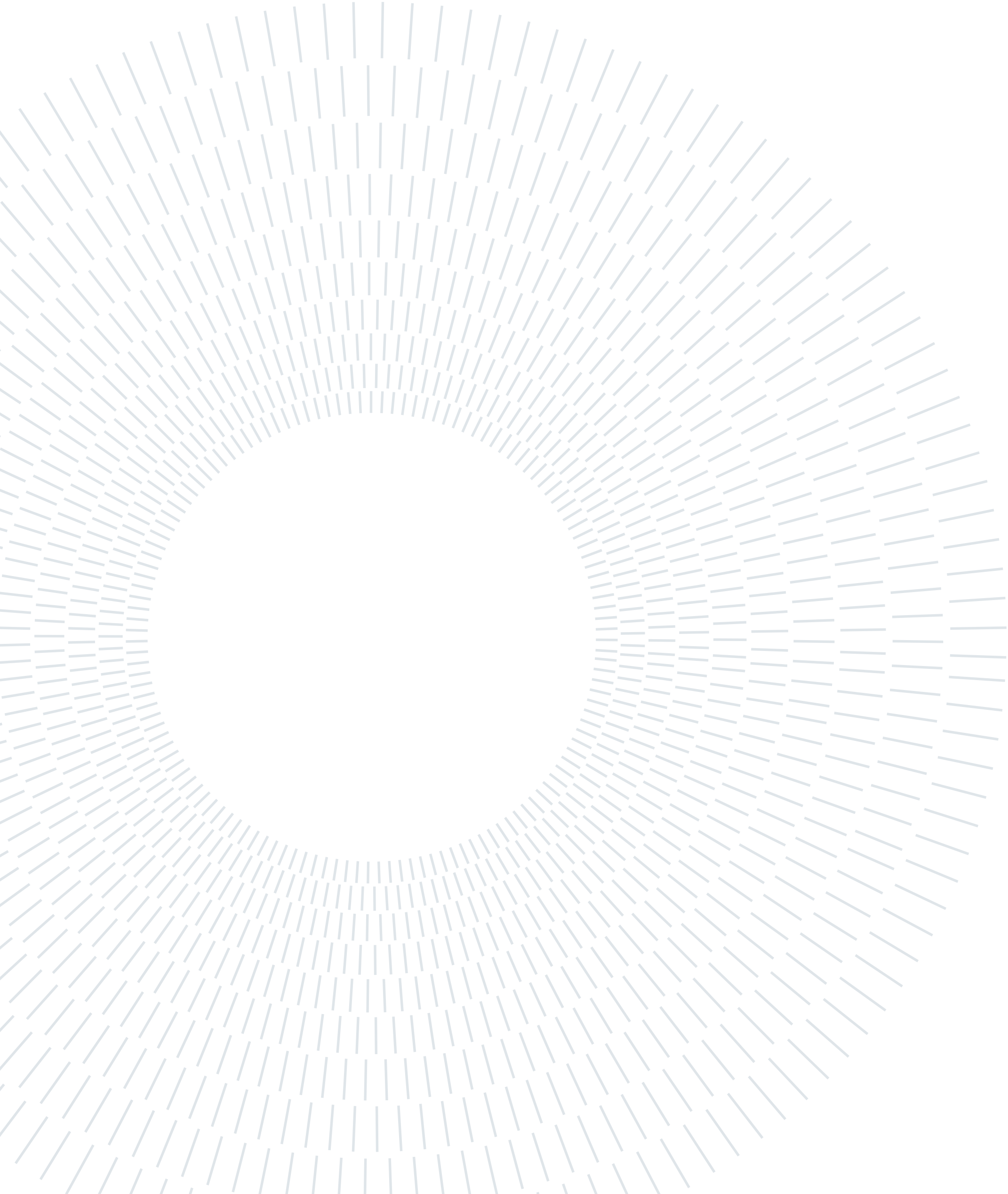

2 | Medical scenario

The considered medical scenario is a vertebral osteotomy. In the following chapter, some details about the structure of a vertebra and the surgical operation are given. In the last section, the mechanical characterization is discussed.

The vertebra [31] is one of the bones that composes the spinal column. The spinal column is divided into several sections, including the cervical spine (neck), thoracic spine (chest), lumbar spine (lower back), sacrum, and coccyx. The vertebra is a complex structure, made of various components, including the vertebral body, vertebral arch, and several bony prominences as shown in Fig 2.1. The vertebral body serves as the primary load-bearing element and is positioned at the anterior aspect of the bone. In contrast, the vertebral arch is located at the posterior side and encloses the spinal canal, which houses the spinal cord. Two of the bony prominences present in a vertebra are the spinous process and the transverse process. The spinous process extends from the posterior aspect of the vertebral arch, while the transverse processes protrude from its lateral aspects.

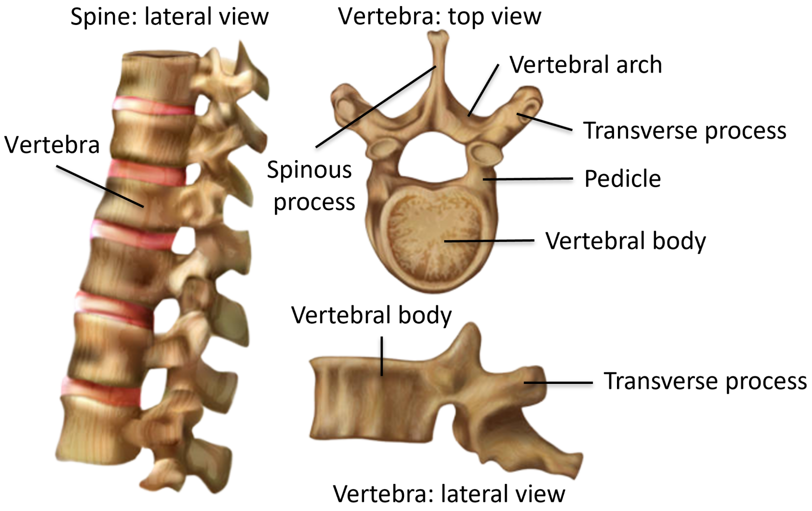
Spine: lateral view
Vertebra: top view
Vertebral arch
Vertebra
Transverse process
Spinous process
Pedicle
Vertebral body
Vertebral body
Transverse process
Vertebra: lateral view

Figure 2.1: High level description of vertebral bones sections

The vertebral body has a cylindrical shape, with a wider transverse dimension than the anterior-posterior direction. The shape and size of the vertebrae vary depending on their location in the spinal column. For example, the vertebrae in the cervical spine are generally smaller and more mobile than those in the thoracic or lumbar spine, which are larger and more stable. The shape and structure of the vertebrae also play an important role in supporting the weight of the body and protecting the spinal cord and nerves (Fig 2.2). These structures are responsible for transmitting signals that enable the brain to control movement and sensations throughout the body. Ensuring that the vertebrae prevent injury and damage to these structures is essential for maintaining the proper functioning of the body.

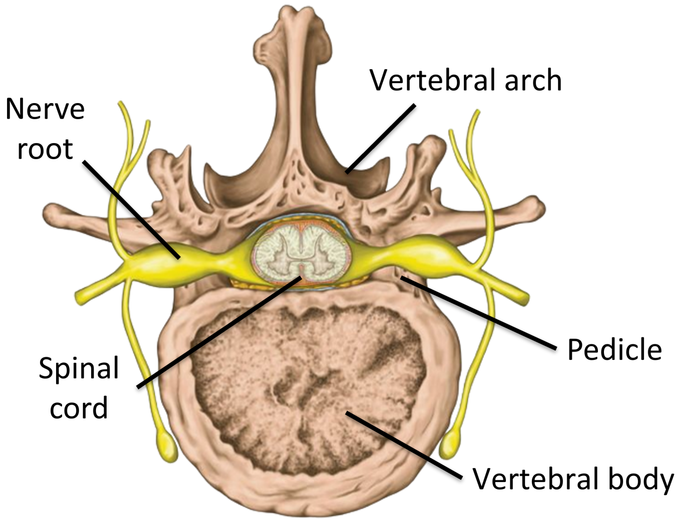

Figure 2.2: Vertebra top view: spinal cord position

Vertebral osteotomy is a surgical procedure that involves cutting and reshaping a vertebral bone to correct a spinal deformity or to improve spinal alignment [32]. This procedure is typically used to treat conditions such as scoliosis, kyphosis, and traumatic or degenerative disorders. During a vertebral osteotomy, the surgeon makes an incision in the patient's back and exposes the affected vertebrae. A portion of the vertebral bone is then removed using specialized surgical instruments, such as bone saws, osteotomes, or drills. The remaining bone is reshaped to achieve the desired correction (Figure 2.3). The part of the vertebra that is typically involved in vertebral osteotomy is the vertebral body, which is the main weight-bearing structure of the vertebra. In some cases, the surgeon may also remove or reshape the spinous processes and/or laminae. Vertebral osteotomy can be used for tumor resection in some cases. The tumor can grow within the vertebral body itself, which may require surgical removal of the affected bone to completely remove the tumor. In these cases, a vertebral osteotomy may be performed to remove the affected portion of the vertebral bone, including the tumor. Note that vertebral osteotomy for tumor resection is a complex procedure that requires a skilled and experienced surgical team.

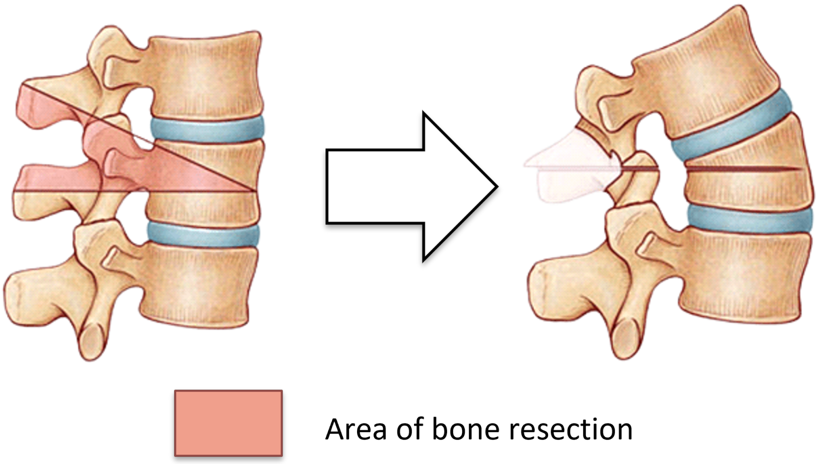

Figure 2.3: Example of the vertebral osteotomy. On the left, the side view of the spine is shown. In red, the area of the vertebra that needs to be cut is represented. On the Right, the improved spine curvature after the osteotomy procedure is shown.

In this procedure, it is important for the surgeon to take great care to avoid damaging nearby tissues, such as the spinal cord, nerves, and blood vessels. The damage of the spinal cord, in particular, can result in serious complications, including paralysis[33]. The surgeon typically uses specialized instruments and imaging techniques, such as intraoperative neuromonitoring to help ensure the safety of the procedure and to avoid damage to critical structures.

These factors can significantly impact the complexity of the procedure, as well as the surgical time required to complete it. As a result, the difficulty level of the operation can vary widely depending on the specific type of osteotomy required. In addition, the high level of precision and safety measures necessary during the procedure can contribute to a significant mental workload and stress for the surgeon. Overall, the classification of vertebral osteotomy is an important consideration in planning the surgical approach and in assessing the potential risks and benefits of the procedure.

2.1. Mechanical characterization

In order to develop a proper control strategy, it is necessary to analyze the mechanical properties of the human body parts involved in the operation. It is particularly important to examine the disparity between their respective Young's moduli, which measures a material's ability to deform under the influence of an applied force. In particular, Young's modulus E is a measure of the stiffness of a material and is defined as the ratio of stress to strain in the linear elastic region of the stress-strain curve. It is a fundamental mechanical property that characterizes the material's ability to resist deformation under load. The Young modulus is expressed as:

$$E = \frac{\sigma}{\epsilon} \tag{2.1}$$

with σ being the tensile stress applied, in terms of force per unit area, and ϵ being the tensile strain, so the extension per unit length.

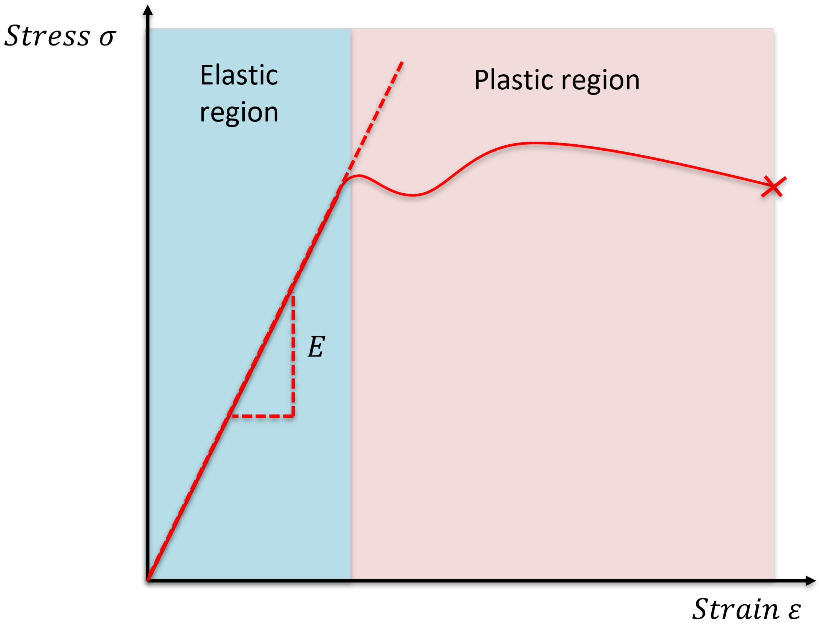

Figure 2.4: Example of a stress-strain curve

Considering a vertebra is mainly composed of cortical bone, which can be associated with a Young modulus $E_b \approx 15 - 20GPa$ [34]. Considering a vascular structure, e.g. a vein, the considered Young modulus is lower, $E_v \approx 2 - 6MPa$ [35].

These ranges will be taken into account in Section 3.4 of Chapter 3 in developing and testing of the control strategy.

3 | Materials and methods

The first section of the chapter discusses the architecture of the Kuka LWR 4+ robot, including a brief overview of its kinematics and dynamic models, an introduction to its primary control strategies, and the Fast Research Interface- In the second section, a description of the sensors involved in the project is provided. Finally, the control strategy is presented, together with the passivity demonstration of the system.

3.1. KUKA LWR IV+

In this project, the KUKA Light-weight Robot 4+ (LWR4+) is used. The LWR [36][37] is an $m = 7$ degree-of-freedom robot arm, initially designed by the German Aerospace Center (DLR) and currently manufactured by KUKA.

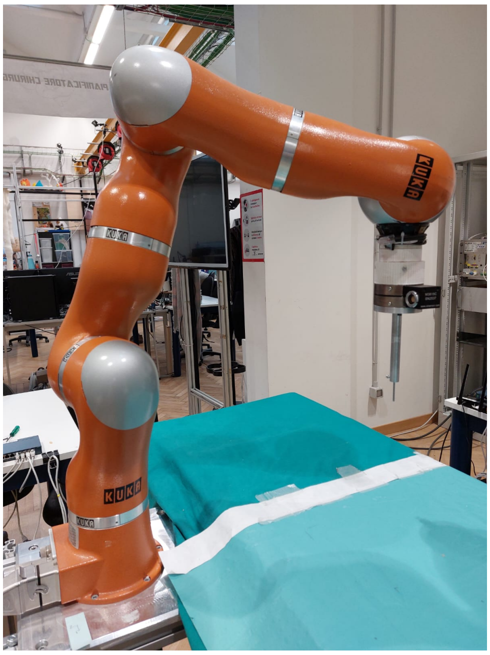

Figure 3.1: Picture of the KUKA LWR4+ at NEARLab

Lightweight robots are smaller, lighter, and can be easily integrated into a variety of workspaces and workflows [38], while traditional industrial robots are typically large, heavy, and require significant safety measures to prevent injury. Their versatility makes them suitable for a broad spectrum of industrial activities, including assembly, inspection, material handling, and packaging, as well as for performing HRI tasks in the medical sector.

The Kuka LWR4+ features brushless motors, harmonic drive gears, and multiple sensors in each joint. Each joint is equipped with position sensors on the motor side, as well as a joint torque sensor. With a weight of around 16 kg and a maximum reach of 936 mm, the LWR is well-suited for a wide range of applications. Additionally, the robot comes with the following pre-installed control strategies:

- Gravity compensation
- Position control
- Impedance control in the joint space
- Impedance control in the Cartesian space

The Kuka LWR has been developed to enable a range of applications that differ significantly from those possible with earlier generations of industrial robots. Unlike traditional industrial robots that excel in high precision, fast motion, robustness, and cost-effectiveness, the LWR is designed to perform operations in unstructured environments and facilitate interaction with human operators. By placing torque sensors in each joint, it becomes possible to develop effective closed-loop control strategies and closely monitor the interaction forces that act on the robot. These sensors are positioned near the joint actuators, enabling them to measure joint vibrations and reduce the impact of inherent joint elasticity. Moreover, the passivity-based nature of these strategies makes it possible to control energy input and maintain system stability, even in unfamiliar environments. Notably, the robot controller's primary control loop can operate at a rate of up to 1 kHz, ensuring the timely and precise execution of commands. The robot is controlled using a computer with Robotic Operating System (ROS) on Ubuntu 16.04, connected to the robot through the Fast Research Interface. In fact, another key feature of lightweight robots is their ease of use and flexibility. They are often designed to be easy to program and operate, using intuitive interfaces and programming languages that can be learned quickly and easily. KUKA Robotics developed the Fast Research Interface (FRI), which is a software interface that allows researchers and developers to directly control the KUKA LWR IV+ robot arm in real-time using a standard computer. Further information on FRI can be found in Section 3.1.3.

3.1.1. Kinematics

In this section, the kinematic model of the Kuka LWR4+ is discussed. The robot is characterized by seven revolute joints. Being $n = 7$ the number of joints and $m = 6$ the degrees of freedom of the end-effector, the degree of redundancy is obtained as $r_d = n - m = 1$. In order to accurately describe the kinematic chain and the reference frames of the robot joints, the Denavit-Hartenberg convention is used: in Tab 3.1 the values of the parameters are reported, while in Fig 3.2 the reference frames are shown, with the robot in its zero configuration.

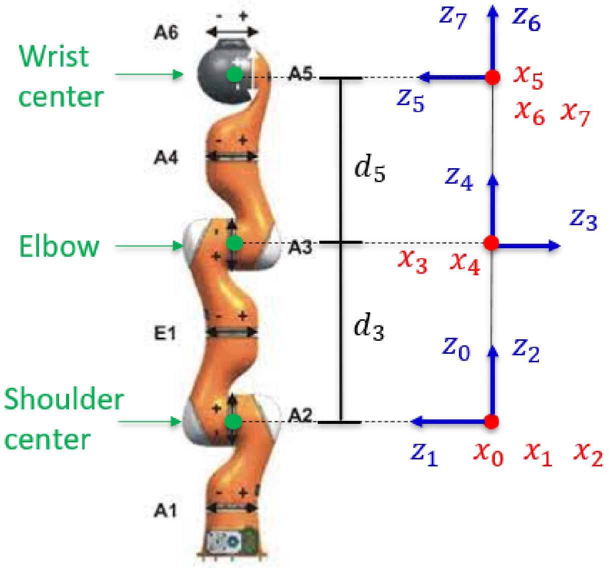
A6
Wrist center
A5
A4
Elbow
A3
E1
Shoulder center
A2
A1
d_5
d_3
z_7
z_6
x_5
z_5
x_6 x_7
z_4
z_3
x_3 x_4
z_0
z_2
z_1 x_0 x_1 x_2

Figure 3.2: DH reference frames

	Joints	d_i(m)	q_i(rad)	a_i(m)	α_i(rad)
J1	A1	0	q_1	0	$\pi/2$
J2	A2	0	q_2	0	$-\pi/2$
J3	E1	0.4	q_3	0	$-\pi/2$
J4	A3	0	q_4	0	$\pi/2$
J5	A4	0.39	q_5	0	$\pi/2$
J6	A5	0	q_6	0	$-\pi/2$
J7	A6	0	q_7	0	0

Table 3.1: DH parameters

Given $\boldsymbol{x}$ the vector of position and orientation of the end-effector in the Cartesian space and $\boldsymbol{q}$ the vector of the joint angle coordinates in the joint space, the forward kinematics relation [39] between them is written as:

$$\boldsymbol{x}(t) = f(\boldsymbol{q}) \tag{3.1}$$

where $\boldsymbol{x}(t) \in \mathbb{R}^m$ and $\boldsymbol{q} \in \mathbb{R}^n$.
Deriving (3.1) it is possible to obtain the differential kinematic:

$$\dot{\boldsymbol{x}}(t) = \boldsymbol{J}(\boldsymbol{q})\dot{\boldsymbol{q}} \tag{3.2}$$

where $\dot{\boldsymbol{x}}\boldsymbol{(t)}$ contains the velocities components of the end-effector, $\boldsymbol{J(q)} \in \mathbb{R}^m \times n$ is the Jacobian matrix. The Jacobian matrix can be interpreted as a linear transformation that, at a given joint configuration $\overline{\boldsymbol{q}}$, maps a vector from $\mathbb{R}^n$ to $\mathbb{R}^m$. In particular, given the input space $\mathbb{R}^n$, it is possible to define two associated subspaces: the range and the null space. The range of $\boldsymbol{J}$, from a physical point of view, represents the joint velocities that are mechanically possible to be generated by the manipulator's drive mechanism. The null space represents the achievable velocities, on the joints, such that a zero end-effector velocity is obtained, in every Cartesian component.

By differentiating again 3.2, the secon-order differential kinematics is obtain:

$$\ddot{\boldsymbol{x}}(t) = \boldsymbol{J}(\boldsymbol{q})\ddot{\boldsymbol{q}} + \dot{\boldsymbol{J}}(\boldsymbol{q}, \dot{\boldsymbol{q}})\dot{\boldsymbol{q}} \tag{3.3}$$

For robotic manipulators, a problem is represented by kinematic singularities. A configuration $\overline{\boldsymbol{q}}$ is said to be singular if the matrix $\boldsymbol{J(\overline{q})}$ is singular. In these configurations, end-effector velocities and accelerations may be impossible to be generated in certain directions, or they exist but are unfeasible for any velocity commanded at the joints.

Regarding the inverse kinematics computation, it consists in deriving a mathematical expression that allows to compute the joint-space variable, given the cartesian space variables of the end-effector. For a non-redundant manipulator, it is possible to invert the previous equations, while for a redundant manipulator, the computation of the Jacobian pseudo-inverse $\boldsymbol{J_{pinv}}$ is required. In general various methods or approximations can be used for this computation.

3.1.2. Dynamic model

In this section, the dynamic model of the robot is discussed.
The Kuka LWR4+ is characterized by flexible joints. Under the modeling assumptions in [2], the entire system, in contact with an environment, can be modeled as follows:

$$\boldsymbol{M_q}(\boldsymbol{q})\ddot{\boldsymbol{q}} + \boldsymbol{C_q}(\boldsymbol{q}, \dot{\boldsymbol{q}})\dot{\boldsymbol{q}} + \boldsymbol{g}(\boldsymbol{q}) + \boldsymbol{K_q}(\boldsymbol{q} - \boldsymbol{\theta}) = \boldsymbol{\tau_{ext}} \tag{3.4a}$$

$$\boldsymbol{B}\ddot{\boldsymbol{\theta}} + \boldsymbol{K}(\boldsymbol{\theta} - \boldsymbol{q}) = \boldsymbol{\tau_m} \tag{3.4b}$$

The two vectors $\boldsymbol{q} \in \mathbb{R}^n$ and $\boldsymbol{\theta} \in \mathbb{R}^n$ represent the link and motor positions. The first equation is characterized by a second-order system on the left side. It describes the dynamics of a rigid body through the following terms: the inertia matrix $\boldsymbol{M_q}(\boldsymbol{q})$, Coriolis matrix $\boldsymbol{C_q}(\boldsymbol{q}, \dot{\boldsymbol{q}})$, gravity vector $\boldsymbol{g}(\boldsymbol{q})$. The term $\boldsymbol{\tau_{ext}}$ represents the external actions acting on the system, which can be related to the force/torque vector applied on the end effector, linked through the relation $\boldsymbol{\tau_{ext}} = \boldsymbol{J^T}(\boldsymbol{q})\boldsymbol{F}$, where $\boldsymbol{J}(\boldsymbol{q})$ is the robot Jacobian. The second equation shows that the torque τ_m is dependent on the stiffness of the corresponding joint and from the joint torque $\boldsymbol{\tau_j} = \boldsymbol{K}_j(\boldsymbol{\theta} - \boldsymbol{q})$. Matrix $\boldsymbol{K_q}$ is the matrix of joint stiffness and it is diagonal and positive definite. Matrix $\boldsymbol{B}$ is the inertia matrix collecting the rotors' inertial components around their spinning axes.

In general, the link and motors equations are dynamically coupled. Mathematically, the coupling is due to $\boldsymbol{\tau_j}$ and a matrix $\boldsymbol{S}(\boldsymbol{q})$ that express the inertial couplings between the rotors and the previous links in the robot chain. Because of the presence of large reduction ratios, the energy contributions due to the inertial couplings between the motors and the links can be neglected. This corresponds to the state that the angular velocity of the rotors is due only to their own spinning, and the model 3.4 can be obtained.

The main characteristic of this model is that the only dynamical coupling happens through the elastic torque $\boldsymbol{\tau_j}$ and the motor equations are expressed through a linear relation. Moreover, other dissipative effects, such as viscous friction at both sides of the transmissions and spring damping of the elastic joints is not considered. In principle, this type of friction can be fully compensated by a suitable choice of control torque. The state of the system can be identified in position and motor speed and joint torques, which are directly measurable.

In the following table, the numerical values of joint position and torque limits are reported.

	q_{min}(degree)	q_{max}(degree)	τ_{max}(Nm)
J1	-170	170	176
J2	-120	120	176
J3	-170	170	100
J4	-120	120	100
J5	-170	170	100
J6	-120	120	38
J7	-170	170	38

Table 3.2: Joint limits

3.1.3. Fast Research Interface

The Kuka LWR manufacturer developed software to enable communication between a remote PC and the robot itself. This is the Fast Research Interface (FRI)[40], which is embedded in industrial commercial controllers.

This interface allows to acquire several information about the robot, such as its state, Jacobian, mass matrix, and position of the robot in the Cartesian space. Moreover, the user can select the desired access rate during the activation of the interface. The control system monitors the quality of communication constantly, once the communication starts.

The robot controller is equipped with the Kuka Control Panel (KCP), shown in Fig. 3.3, which gives the user access to different operating modes. In this way, the user can interact with the robot to test the programmed operations and can perform them with increased safety. The controller is characterized by its own language: Kuka Robot Language (KRL). To edit, display and execute KRL scripts, the panel can be used.

Figure 3.3: Kuka Control Panel

The Kuka motion kernel provides different methods to generate pre-defined trajectories by simple KRL commands. FRI interacts directly with the motion kernel: these trajectories can be sent to the remote pc and modified. Moreover, since an impedance controller is already available on the Kuka, it is possible to send a command that modifies the stiffness and damping parameters of the impedance controller.

FRI allows also to use of generic variables to read or write digital I/O of the KRC, to control the tool mounted on the robot end-effector, to read internal states to the KRL program or to change the program flow of KRL scripts.

The communication between the remote pc and the controller uses a UDP protocol. Since usually real-time communication between the remote pc and controller is required, it is necessary to detect every packet loss and to monitor and measure the communication delays and variations. So, the interface uses UDP sockets and implements its own packet loss detecting and recovering mechanism.

FRI activation can be represented as a state machine (Fig 3.4) and has two modes: Monitor (data provided, no cyclic commanding) and Command (data provided, cyclic commanding required). When activated, FRI enters monitor mode and the KUKA controller sends data to the remote computer, which must respond with commands within a given timeframe to enter command mode.

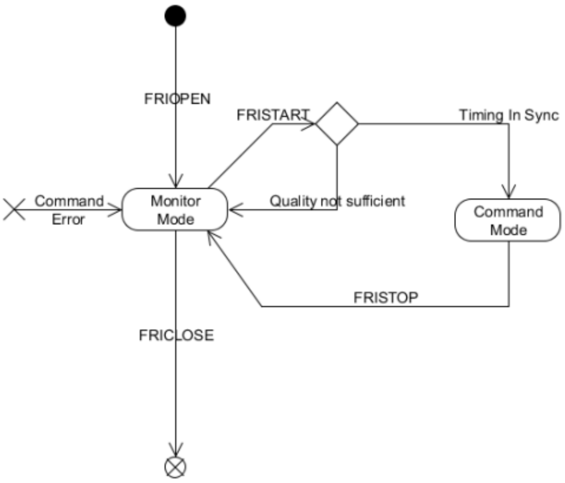

Figure 3.4: FRI state machine with monitor and command mode

In the context of usability, it is important to take into account safety concerns, including both machine and user safety. As the system originates from industrial controllers, it supports the "test" and "automatic" operating modes. During test mode, a three-way engage switch is activated, enabling the user to test the software and immediately stop the robot in the event of any obviously erroneous behavior.

To ensure safety, the remote site must comply with these safety modes and be informed of the system's activities. Additionally, joint speeds are closely monitored and restricted. To test the interface and gain experience, the user can reduce the allowable limits for FRI, ensuring that the robot will not execute erroneous commands. If the commanded values exceed the limits or the timing requirements are not met, the KRC will enforce a fallback to "monitor mode" and bring the robot to a safe state.

Control modes

In this section, the control modes available from the Kuka manual[41] are discussed, with the notation used in the manual.

The first cyclic control mode available is the Joint specific position control. The command is interpreted as follow:

$$\boldsymbol{q}_{cmd} = \boldsymbol{q}_{FRI} \tag{3.5}$$

This means that the original command, from the KRC, is replaced by the external command $\boldsymbol{q_{FRI}}$

Considering the Joint specific impedance control, the control law is the following:

$$\boldsymbol{\tau_{cmd}} = \boldsymbol{K_j(q_{FRI} - q_{msr}) + D(D_j) + \tau_{FRI} + f_{dynamics}(q, \dot{q}, \ddot{q})} \tag{3.6}$$

being $\boldsymbol{K_j}$ the joint stiffness diagonal matrix, $\boldsymbol{D_j}$ the normalized diagonal damping matrix, $\boldsymbol{q_{FRI}}$ the desired joint positions vector, and $\boldsymbol{\tau_{FRI}}$ the superposed control torque, all modifiable from the remote side. The damping term $\boldsymbol{D(d_j)}$ and the dynamic model $\boldsymbol{f_{dynamics}(q, \dot{q}, \ddot{q})}$ are computed internally.

Finally, the Cartesian impedance control law is defined as follows:

$$\boldsymbol{\tau_{cmd}} = \boldsymbol{J^T(K_c(x_{FRI} - x_{msr}) + D(D_c) + F_{FRI}) + f_{dynamics}(q, \dot{q}, \ddot{q})} \tag{3.7}$$

with $\boldsymbol{J^T}$ the transposed Jacobian matrix. Considering the other parameters: $\boldsymbol{K_c}$ is the Cartesian diagonal stiffness matrix, $\boldsymbol{D_c}$ is the normalized damping, $\boldsymbol{x_{FRI}}$ is the Cartesian pose, $\boldsymbol{F_{FRI}}$ is the superposed Cartesian force/torque term, and they are all modifiable if desired. Finally, the damping term $\boldsymbol{D(D_c)}$ and the dynamic model $\boldsymbol{f_{dynamics}(q, \dot{q}, \ddot{q})}$ are taken care inside the motion kernel.

As a final note, here's the list of available data that a remote computer can access from the KRC:

- Joint sensor data, both position, and torque
- Cartesian measured data, both pose and estimated force/torque
- Information about interface state
- Information about robot state
- Current commanded values
- Current Jacobian matrix and mass matrix
- KRL interaction variables

3.2. Sensors

This section provides an overview of the sensors incorporated into the project, namely a six-axis force/torque sensor and the MyoWristband EMG sensor.

3.2.1. Force Sensor

Force/torque sensors are a type of sensor that measures the three components of force and the three components of the moment with respect to a local reference frame. The way the measurement is performed is based on strain gauges, for which given a strain, tension, or compression applied, a variation in an electric circuit is caused, in particular in the resistance. From the electric signal, it is possible to compute the force and torque components.

The equipped force sensor is a M3815C six-axis force/torque load cell produced by Sunrise Instruments.

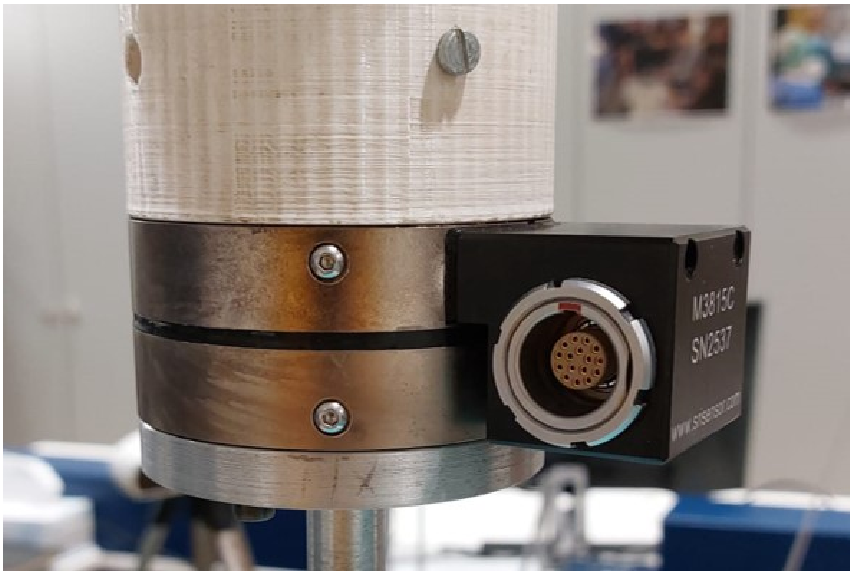

Figure 3.5: 6 axis force/torque sensor, mounted on the KUKA

To improve the accuracy of the force sensor measurements, an exponential smoothing filter was applied to the raw sensor readings, which are characterized by a sampling time of 1000 Hz. The filter equation used is given by:

$$\boldsymbol{F_{filt}} = \alpha_f \boldsymbol{F_{raw}} + (1 - \alpha_f)\boldsymbol{F_{filt}(t-1)} \tag{3.8}$$

where $\boldsymbol{F_{filt}}$ and $\boldsymbol{F_{raw}}$ represent the filtered and raw force values respectively, t denotes the current time step, and α_f is the smoothing factor. The exponential smoothing filter uses an exponential window function to smooth the time series data. A larger value of α_f results in less smoothing effect, as the output series becomes closer to the current observation (i.e., $\alpha_f = 1$). Conversely, when α_f is close to zero, the filter has a greater smoothing effect, but it is less responsive to recent changes in the force readings. The value of α_f was determined empirically and set to 0.05, resulting in a cutoff frequency of 50 Hz.

Then, to align the reference frame of the force sensor with the one of the end-effector,a rotation matrix around the z-axis with an angle of θ of 20° was performed. This enabled the force sensed by the force sensor to be expressed in the reference frame of the last joint. Given F_{J7} and F_{fs} the reference frame of the end-effector and force sensor, respectively, the rotation between the two frames can be expressed as:

$$F_{J7} = \begin{bmatrix} \cos\theta_r & -\sin\theta_r & 0 \\ \sin\theta_r & \cos\theta_r & 0 \\ 0 & 0 & 1 \end{bmatrix} F_{fs} \tag{3.9}$$

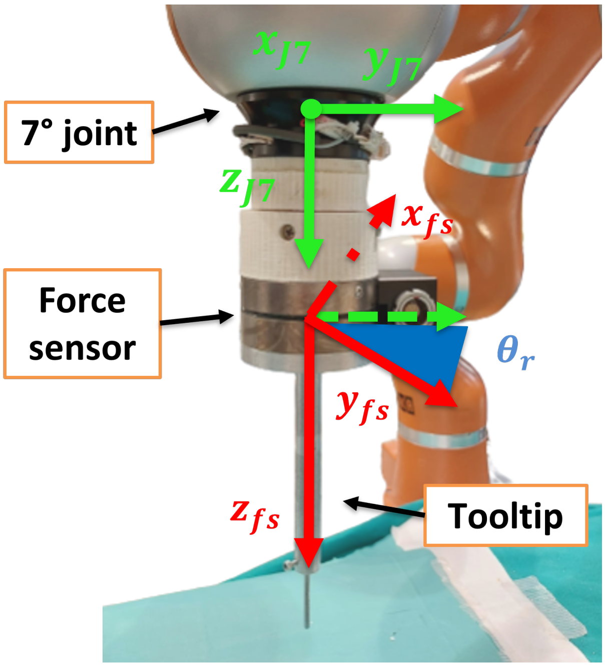

Figure 3.6: Representation of the calibration. In green, the reference frame of the seventh joint is shown. In red, the sensor frame of the force sensor is shown, rotated by an angle θ_r around the z-axis.

Finally, the effect of the tool weight on the force measurement was removed. Since the contribution of the tool gravity depends on the orientation of the end-effector, the relationship between the force read and the end-effector orientation is non-linear. For this reason, a MultiLayer Perceptron Regressor with one layer composed of 30 neurons was trained (Figure 3.7). The network takes the end-effector orientation as input and predicts the force read by the force sensor after removing the tool gravity contribution $\boldsymbol{F_{ee_x}}, \boldsymbol{F_{ee_y}}, \boldsymbol{F_{ee_z}}$. The chosen activation function was the Rectified Linear Unit (ReLU), and the network was trained using the Adam solver with a learning rate of 0.01 and an alpha of 0.01. The network was trained with a dataset containing 14,926 data points. The orientation of the end effector was used as input, and the force sensor readings as output. The dataset was collected with the robot in gravity compensation mode and 30% of the data was used for testing. After the training, the network takes as input the orientation of the end effector and predicts the force read by the force sensor $\boldsymbol{F_{ee}}$, without the tool gravity contribution.

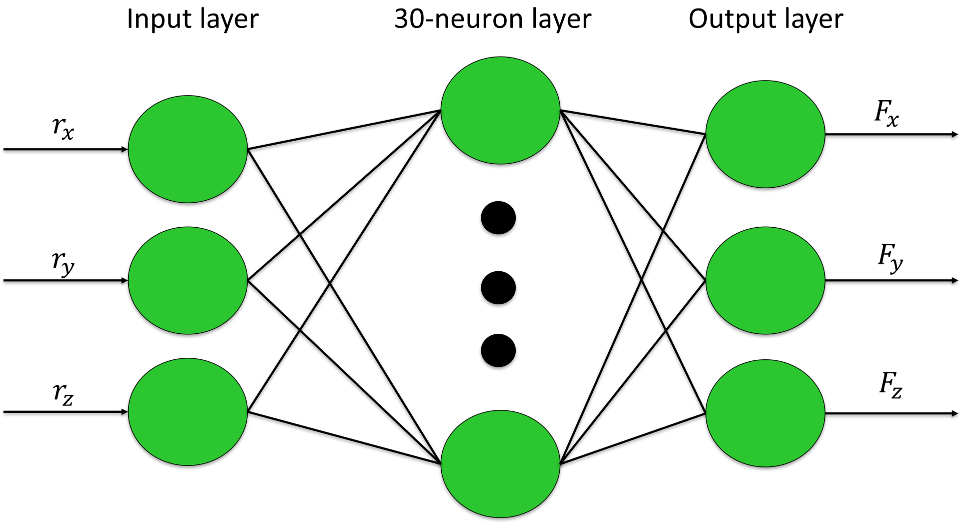

Figure 3.7: Scheme of the Multilayer Perceptron Regressor. Input: orientation of the end effector. Output: component x, y, z of the force sensor.

In Figure 3.8, the processing of the sensor readings is represented.

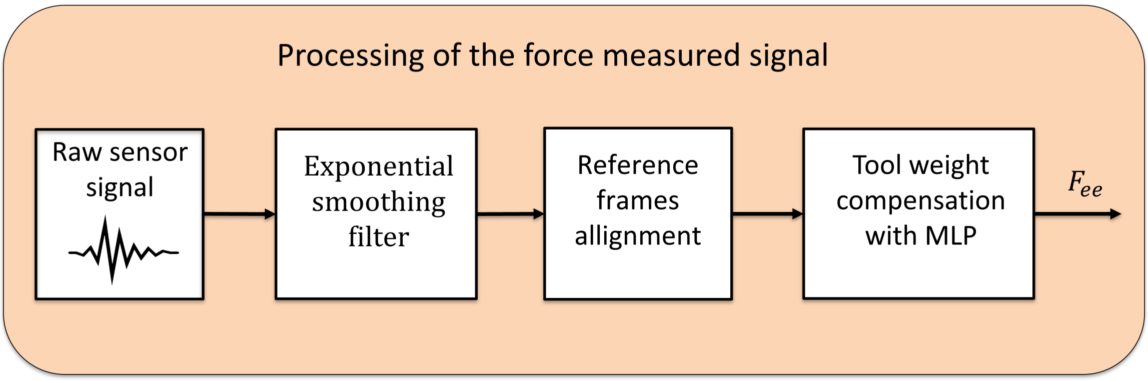
Processing of the force measured signal
Raw sensor signal
Exponential smoothing filter
Reference frames allignment
Tool weight compensation with MLP
F_{ee}

Figure 3.8: Scheme of the processing of the force signal: first an exponential smoothing filter is applied. Next, The sensor reference frame is aligned with the frame of the seventh joint. Then, the tool weight is compensated using a Multilayer Perceptron regressor.

3.2.2. Emg sensor: MyoWristband

An electromyogram (EMG) captures the electrical signals generated by muscle contractions, which are controlled by the nervous system.
In this project, the Myo Wristband is adopted as EMG sensor.

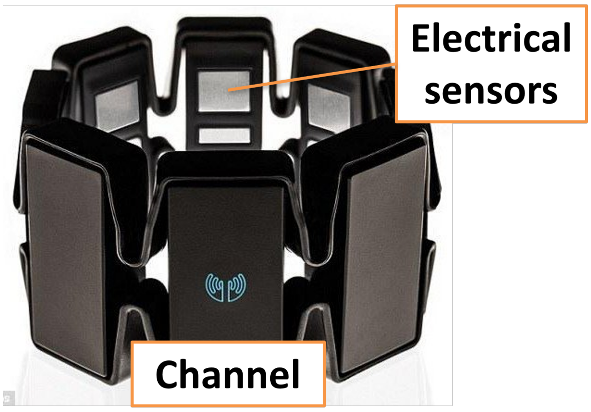
Electrical sensors
Channel

Figure 3.9: MyoBand electromyography sensor

The Myo Wrist Band (Myoband) is a bracelet produced by Thalmic Lab, equipped with 8 channels (Figure 3.9), used to elaborate the electric signals produced by the muscles in the forearm. The sensor communicates with the user's computer through Bluetooth, and can be connected to ROS to elaborate the data. The 8 EMG raw signals have a sample rate of 200 Hz and are processed by the sensor itself: the absolute value of the signal was obtained with a full wave rectification and a low pass filter with a 50 Hz cutoff frequency was applied to extract the envelope of the original signal. As the user wears the MyoWristBand, muscle activity can be elaborate in order to produce an estimate of the force applied by the user $\boldsymbol{F_h}$, in order to introduce this signal in the main control scheme. This idea is supported by the fact that, in HRI, it is extremely useful to evaluate human intentions. In Figure 3.10, a scheme of the processing phases of the EMG signal is reported.

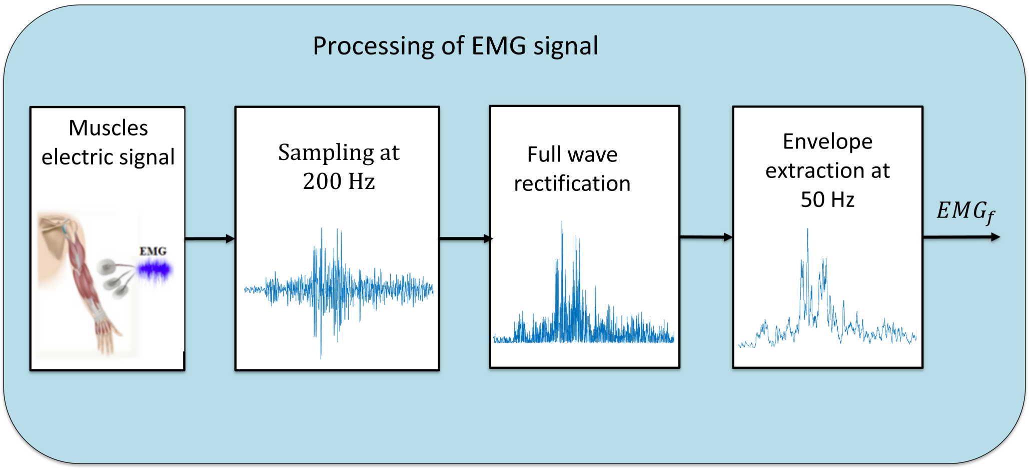
Processing of EMG signal
Muscles electric signal
EMG
Sampling at 200 Hz
Full wave rectification
Envelope extraction at 50 Hz
EMG_f

Figure 3.10: Scheme of the EMG signal processing. First, the muscle signals are sampled at 200 Hz. Then, a full wave rectification is applied and the signal envelope is extracted at 50 Hz.

In Figure 3.11, an example of the 8 filtered signals $\boldsymbol{EMG_f}$ is shown.

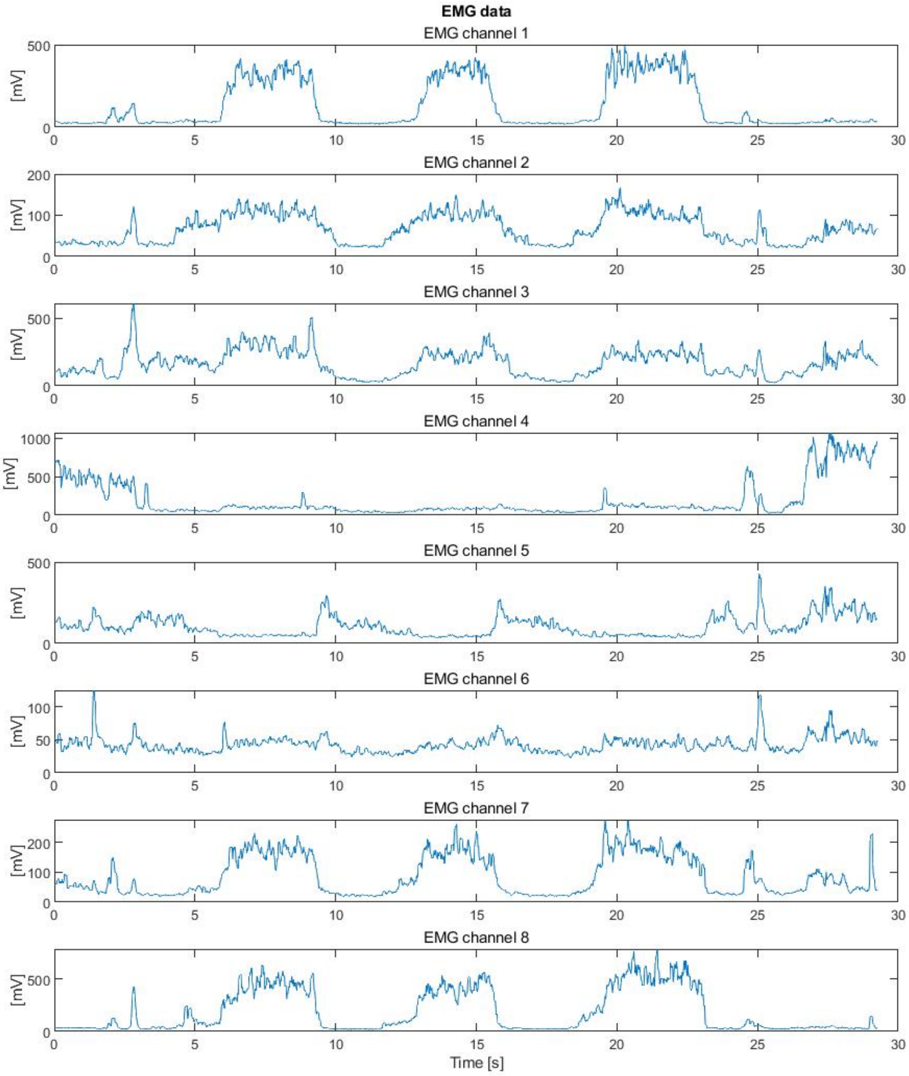

Figure 3.11: EMG processed signals for the 8 channels of the forearm muscle activity.

Estimation of human force

In this section, the process of human force estimation is discussed. The goal is to train an offline model that can accurately map the signals of the EMG signal into a force vector $\boldsymbol{F_h}$:

$$\boldsymbol{F_h} = \Phi(\boldsymbol{EMG_f}) \tag{3.10}$$

where $\boldsymbol{EMG_f}$ are output signals of the 8 channels, already filtered. Once the model is trained offline, it can be used online to evaluate the user's force applied to the robot.

A dataset of approximately 14,000 data points was collected from users wearing the MyoWristband on their forearm and placing their elbow on a steady constraint, as shown in Figure 3.12, and divided into a training set (80%) and a testing set (20%). During the acquisition of the dataset, users were instructed to grab the robot and move it along the x, y, and z axes, while the force on the end-effector was measured by a force sensor. The training set was first normalized using MinMaxScaler so that all data fall within the same range, i.e. between 0 and 1. Next, a linear regression was used to weigh the contributions of the EMG channels. The processed data was then used to train a neural network, consisting of two LSTM layers with 100 units and a "relu" activation function, one dropout layer, two dense layers with 64 and 32 units, both with a "relu" activation function, and one final dense layer with one unit and a sigmoid activation function. The model was trained for 500 epochs and the Adam optimizer was used. The Mean Squared Error (MSE) loss function was used to evaluate the performance of the network.

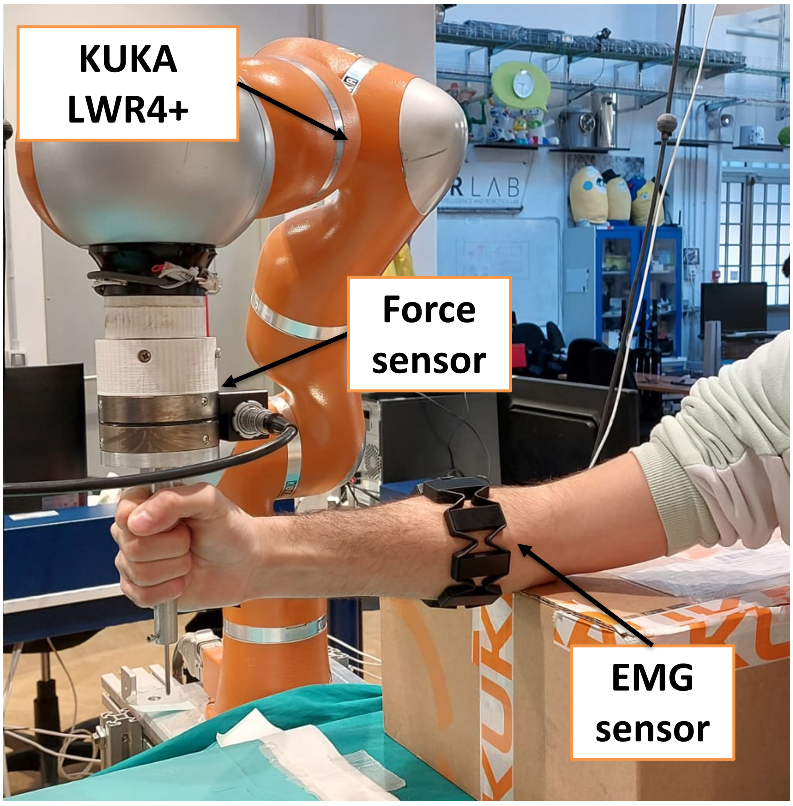

Figure 3.12: The configuration used in the data collection process

3.3. Control Strategy

In the following section, the proposed control strategy is discussed. First, an introduction to the theory of impedance control is reported. Next, the control strategy is described, together with the stability proof.

3.3.1. Theory and modeling of impedance control

Impedance control [13] is a method for controlling the interaction between a robot and its environment. In impedance control, the robot is modeled as a mechanical impedance that interacts with the environment. The impedance is characterized by three parameters: stiffness, damping, and inertia. Stiffness refers to the resistance of the robot to deformation, damping refers to the dissipation of energy in the system, and inertia refers to the resistance of the robot to changes in motion.

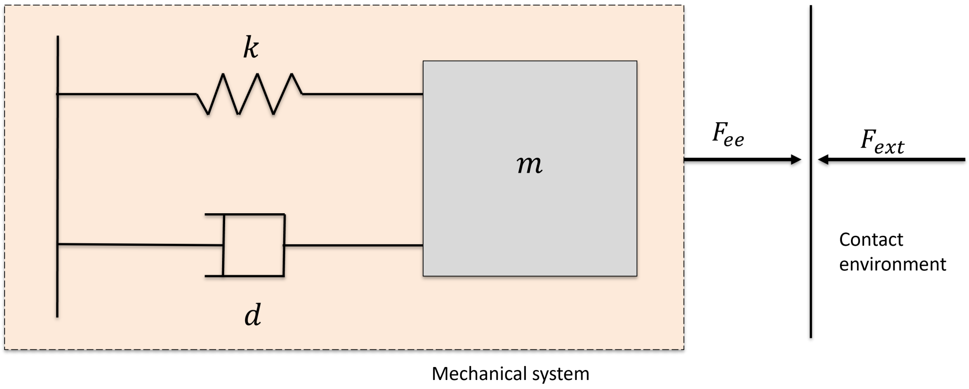

Figure 3.13: 1DOF impedance model representation. k, d and m represent the robot stiffness, damping and inertia, respectively. F_{ee} is the force exherted from the robot end effector on the environment, while F_{ext} is the external force acting on the robot.

The goal of impedance control is to control the interaction between the robot and the environment by adjusting the stiffness, damping, and inertia of the robot's impedance. By changing these parameters, the robot can respond to external forces in a way that is appropriate for the task at hand. For example, if the robot is grasping an object, it may need to adjust its stiffness and damping to prevent the object from slipping or dropping. In an HRI hands-on procedure, impedance control can be used to obtain a robot behavior compliant with the user's will.

Admittance control is a related method, based on the concept of admittance, which is the inverse of impedance. Admittance control involves measuring the force applied to the robot by the environment and using this information to adjust the robot's motion. The robot is modeled as an admittance that interacts with the environment, and the admittance is characterized by the same three parameters as the impedance.

In Figure (3.14), both control logic are represented.

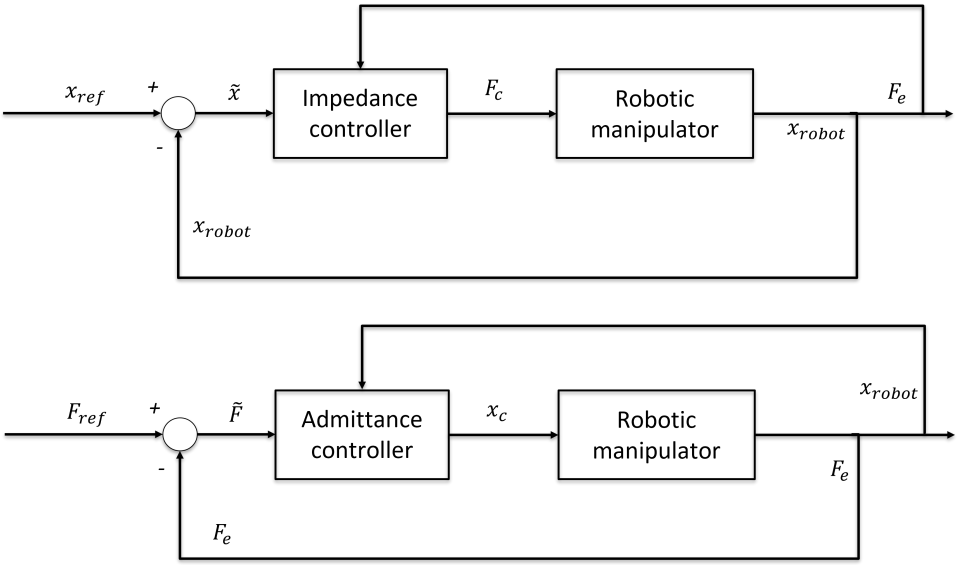
x_{ref}
+
$\tilde{x}$
Impedance controller
F_c
Robotic manipulator
F_e
x_{robot}
-
x_{robot}
F_{ref}
+
$\tilde{F}$
Admittance controller
x_c
Robotic manipulator
x_{robot}
F_e
-
F_e

Figure 3.14: Schemes of Impedance (upper) and Admittance (lower) control logic. In Impedance control, given a position reference, the position error is changed into a force signal. Conversely, an admittance controller receives as input a force error and gives as output a position.

Both impedance control and admittance control are widely used in robotics and have applications in a range of industries, including manufacturing, healthcare, and aerospace. These methods allow robots to interact with their environment in a way that is safe, effective, and appropriate for the task at hand.

Considering the transfer functions, in the case of impedance control:

$$Z(s) = \frac{F(s)}{V(s)} = ms^2 + ds + k, \tag{3.11}$$

while considering admittance control:

$$Y(s) = \frac{V(s)}{F(s)} = \frac{1}{ms^2 + ds + k} \tag{3.12}$$

Note that, even though the definition expresses a relation between the force vector and the velocity vector, in principle the relation can be expressed also between the force and the position/orientation in both the joint space and the Cartesian space.

Considering the Cartesian space, the end-effector dynamic of the robot is:

$$\boldsymbol{M_x}\ddot{\boldsymbol{x}} + \boldsymbol{C_x}\dot{\boldsymbol{x}} + \boldsymbol{g_x} = \boldsymbol{F_c} + \boldsymbol{F_{ext}} \tag{3.13}$$

$\boldsymbol{x} \in \mathbf{R}^n$ is the vector of end-effector pose, with $n = 6$, $\boldsymbol{M_x} \in \mathbf{R}^{n\times n}$ is the inertia matrix, $\boldsymbol{C_x} \in \mathbf{R}^{n\times n}$ is the matrix of the end-effector's Coriolis and centrifugal terms, $\boldsymbol{g_x} \in \mathbf{R}^n$ is the vector of the gravitational wrench and $\boldsymbol{F_c} \in \mathbf{R}^{\boldsymbol{n}}$ is the control wrench in the Cartesian space, $\boldsymbol{F_{ext}} \in \mathbf{R}^n$ is the external force.

The desired impedance behavior can be written as:

$$\boldsymbol{M}_d(\ddot{\boldsymbol{x}} - \ddot{\boldsymbol{x}}_d) + \boldsymbol{D}_d(\dot{\boldsymbol{x}} - \dot{\boldsymbol{x}}_d) + \boldsymbol{K}_d(\boldsymbol{x} - \boldsymbol{x}_d) = \boldsymbol{F_{ext}} \tag{3.14}$$

$\boldsymbol{M_d} \geq 0$, $\boldsymbol{D_d} \geq 0$, $\boldsymbol{K_d} > 0 \in \mathbf{R}^{n\times n}$ are the inertia, damping and stiffness matrix, while $\boldsymbol{x_d} \in \mathbf{R}^n$ is the desired end-effector pose, $\dot{\boldsymbol{x}}_{\boldsymbol{d}} \in \mathbf{R}^n$ is the desired velocity, $\ddot{\boldsymbol{x}}_{\boldsymbol{d}} \in \mathbf{R}^n$ is the desired end-effector. So, the interaction is characterized by the user-chosen impedance parameters of equation 3.14. In HRI tasks, $\boldsymbol{x_d}$ is the free Cartesian rest position, while no acceleration and velocity reference is used. Usually, the impedance parameters are all diagonal matrices, allowing the decoupling of the model according to the Cartesian axis $i \in [1, ..n]$.

In many application, an adaptive rule is used to adjust the impedance parameters, based on the task at hand:

$$\boldsymbol{M}_d(\boldsymbol{t})\ddot{\boldsymbol{x}} + \boldsymbol{D}_d(\boldsymbol{t})\dot{\boldsymbol{x}} + \boldsymbol{K}_d(\boldsymbol{t})(\boldsymbol{x} - \boldsymbol{x}_d) = \boldsymbol{F_{ext}} \tag{3.15}$$

3.3.2. Proposed control strategy

The goal of the proposed strategy was to change the impedance parameters of the robot according to the material that is in contact with the end-effector. Considering the medical scenario of vertebral osteotomy described in Chapter 2, a compliant behavior is required as long as the end-effector is in contact with a material with a high Young's modulus, such as a vertebra. On the other hand, an increase in the robot stiffness is required whenever contact with a material with a low Young's modulus is detected.

In this study, a variable impedance control scheme was developed. In Fig. (3.15), a conceptual scheme of the overall system is reported.

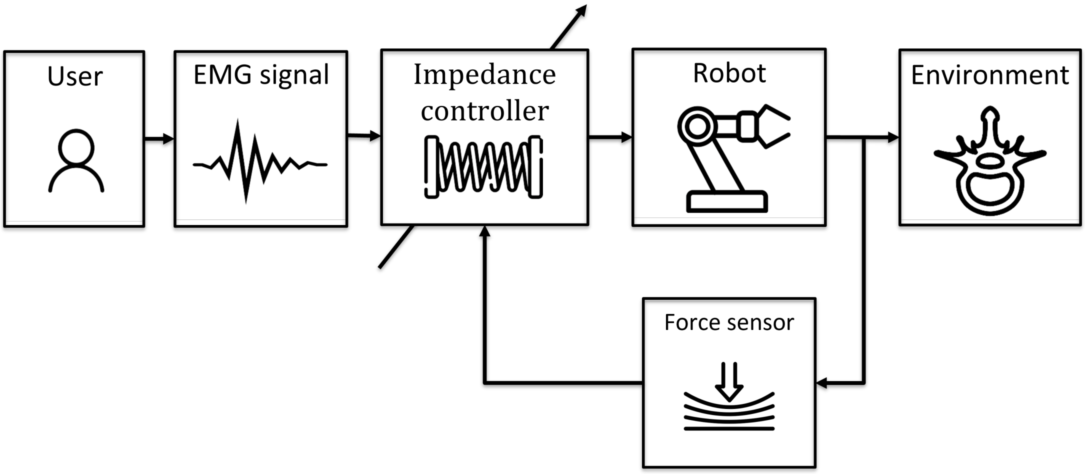

Figure 3.15: Conceptual scheme of the system: impedance parameters are adapted based on the EMG signals and the measured contact force between the robot and the environment.

The main control loop (Figure 3.16) was represented by a Cartesian impedance controller: given as input a position setpoint $\boldsymbol{x}_{ref}$ in the Cartesian space, a torque command $\boldsymbol{\tau}_{cmd}$ in the joint space is generated according to:

$$\boldsymbol{\tau}_{cmd} = \boldsymbol{J}_{pin}^{-1}(\boldsymbol{K}(\boldsymbol{x}_{ref} - \boldsymbol{x}_{curr}) + \boldsymbol{D}(\boldsymbol{D}_n, \dot{\boldsymbol{x}}_{curr})) + \boldsymbol{f}_d(\boldsymbol{q}, \dot{\boldsymbol{q}}, \ddot{\boldsymbol{q}}) \tag{3.16}$$

with $\boldsymbol{J}_{pin}^{-1} \in \mathbf{R}^{m \times n}$ the pseudo-inverse of the Jacobian matrix. $\boldsymbol{K} \in \mathbf{R}^{n \times n}$ is the Cartesian stiffness, $\boldsymbol{D_n} \in \mathbf{R}^{n \times n}$ is the Cartesian normalized damping, $\boldsymbol{x_{ref}}$ is the Cartesian reference pose, given by the difference between the position displacement imposed by the human $\boldsymbol{x_h} \in \mathbf{R}^n$ and the additional feedback $\boldsymbol{x_s} \in \mathbf{R}^n$. $\boldsymbol{x_{curr}} \in \mathbf{R}^n$ is the current Cartesian pose, while $\boldsymbol{q}, \dot{\boldsymbol{q}}, \ddot{\boldsymbol{q}} \in \mathbf{R}^{m \times m}$ are the vectors of robot joint position, velocity, and acceleration, respectively. The Cartesian damping contribute $\boldsymbol{D}(\boldsymbol{D_n}, \dot{\boldsymbol{x}}_{\boldsymbol{curr}})$ and the inertial contribute in the joint space $\boldsymbol{f_d}(\boldsymbol{q}, \dot{\boldsymbol{q}}, \ddot{\boldsymbol{q}})$ are computed by the robot internal controller. According to the value of matrices $\boldsymbol{K}$ and $\boldsymbol{D}_n$, the robot can be more or less compliant with respect to the user's intention.

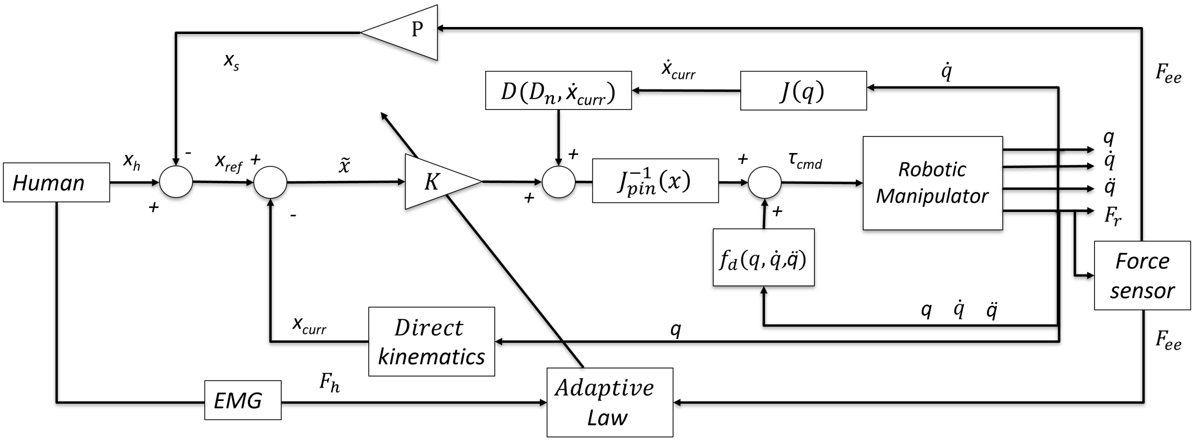

Figure 3.16: Scheme of the adaptive impedance control law with safety position feedback: the Cartesian reference pose $\boldsymbol{x_{ref}}$ is obtained as the difference between the position imposed by the human $\boldsymbol{x_h}$ and the safety position feedback $\boldsymbol{x_s}$, generated by multiplying $\boldsymbol{F_{ee}}$ and the gain matrix $\boldsymbol{P}$. The position error $\boldsymbol{\tilde{x}}$ is then calculated by subtracting $\boldsymbol{x_{ref}}$ and the current Cartesian pose, $\boldsymbol{x_{curr}}$. This error is multiplied by a variable stiffness matrix $\boldsymbol{K}$, controlled by an adaptive law which receives the human estimated force, $\boldsymbol{F_h}$, derived from an EMG signal and the contact force measured by the force sensor, $\boldsymbol{F_{ee}}$, as inputs. $\boldsymbol{F_{ee}}$ is measured from the force $\boldsymbol{F_r}$ that the robot exherts on the environment. The current Cartesian velocity, $\boldsymbol{\dot{x}_{curr}}$, is used to compute the damping term $\boldsymbol{D(D_n, \dot{x}_{curr})}$, where $\boldsymbol{D_n}$ is the normalized damping matrix. The torque command in the joint space $\boldsymbol{\tau_{cmd}}$ is generated by using the Jacobian pseudo-inverse $\boldsymbol{J_{pin}^{-1}}$ and summing the inertial term $\boldsymbol{f}_d(\boldsymbol{q}, \boldsymbol{\dot{q}}, \boldsymbol{\ddot{q}})$, $\boldsymbol{q}, \boldsymbol{\dot{q}}, \boldsymbol{\ddot{q}}$ are the vectors of robot joint position, velocity, and acceleration, respectively.

Considering the adaptive law, the stiffness $\boldsymbol{k}_z$ was changed at every time instant according to the following formula:

$$\boldsymbol{k}_z = k_0 + \boldsymbol{\gamma}(k_1 - k_0) \tag{3.17}$$

where k_1 and k_0 are the limits of range in which the stiffness parameter is allowed to change. $\boldsymbol{\gamma} = \boldsymbol{\gamma}(\boldsymbol{F}_h, \boldsymbol{F_{ee_z}})$ is a variable gain, such that $0 \leq \boldsymbol{\gamma} \leq 1$ $\forall t$, function of both the user's estimated force $\boldsymbol{F}_h$ and the end-effector measured force $\boldsymbol{F_{ee_z}}$:

$$\boldsymbol{\gamma} = \boldsymbol{\gamma}(\boldsymbol{F_h}, \boldsymbol{F_{ee}}) \tag{3.18}$$

In order to obtain the desired stiffness behavior in all situations, two different $\boldsymbol{\gamma}$ profiles were developed:

$$\gamma_1(\boldsymbol{F}_h, \boldsymbol{F}_{\boldsymbol{ee_z}}) = \frac{\alpha|\boldsymbol{F}_{\boldsymbol{ee_z}}|}{\alpha|\boldsymbol{F}_{\boldsymbol{ee_z}}| + ||\boldsymbol{F}_{\boldsymbol{ee_z}}| + \boldsymbol{F}_h|} \tag{3.19}$$

$$\boldsymbol{\gamma_2}(\boldsymbol{F}_h, \boldsymbol{F}_{\boldsymbol{ee_z}}) = \frac{\frac{1}{\alpha}|\boldsymbol{F}_{\boldsymbol{ee_z}}|}{\frac{1}{\alpha}|\boldsymbol{F}_{\boldsymbol{ee_z}}| + ||\boldsymbol{F}_{\boldsymbol{ee_z}}| - \boldsymbol{F}_h|} \tag{3.20}$$

with α being a user-chosen tunable parameter.
In the absence of any contact between the tooltip and the environment, the end-effector measured force was negligible ($\boldsymbol{F}_{\boldsymbol{ee_z}} \approx 0$) and hence $\boldsymbol{k_z}$ remained close to k_0, resulting in a highly compliant robot. When encountering a material with a high Young's modulus, $\boldsymbol{\gamma_1}$ was maintained to keep the robot stiffness, $\boldsymbol{k_z}$, low and compliant during the procedure. In contrast, when the robot made contact with a material with a low Young's modulus, such as a vein or spinal cord, $\boldsymbol{\gamma_2}$ was engaged, increasing the stiffness $\boldsymbol{k_z}$ to reduce the risk of material damage. To differentiate between environments with high/low Young's modulus, a threshold, F_{tresh}, on the contact force was used. However, the condition $|\boldsymbol{F}_{\boldsymbol{ee_z}}| < F_{treshold}$ was satisfied during the initial phase of contact with both material types and was insufficient to differentiate between them. The key difference between the materials was their response to forces. A material with high Young's modulus remained undamaged, while one with low Young's modulus started deforming. For this reason, the displacement ϵ was defined such that, if $|z_{contact} - \boldsymbol{z_{curr}}| > \epsilon$ the material with low Young's modulus was damaged, with $\boldsymbol{z_{curr}}$ the z component of the position vector of the end-effector and $z_{contact}$ the position in which $|\boldsymbol{F}_{ee_z}| > 0$. A position threshold, z_{tresh}, was chosen such that $\epsilon > z_{tresh}$ and when $|z_{contact} - \boldsymbol{z_{curr}}| > z_{tresh}$ and $|\boldsymbol{F}_{\boldsymbol{ee_z}}| < F_{treshold}$, $\boldsymbol{\gamma_2}$ was used. In this way, the stiffness $\boldsymbol{k_z}$ was increased in order to reduce the compliantness of the robot. In Figure 3.17, a scheme of the four possible contact situations is represented. In a real scenario, cases 1a and 2a correspond to the situations in which the surgeon is drilling a vertebra. Case 1b represents the first phase of the contact for both materials, while case 2b represents the contact with a material with low Young's modulus.

In the hypothesis of an error in the procedure, it may become necessary for the robotic system to counteract the user's movements to prevent damage to an unintended structure. To accomplish this, an additional position command, proportional to $\boldsymbol{F}_{\boldsymbol{ee_z}}$, was generated by the controller:

$$\boldsymbol{z}_s = \rho \boldsymbol{F}_{\boldsymbol{ee_z}} \tag{3.21}$$

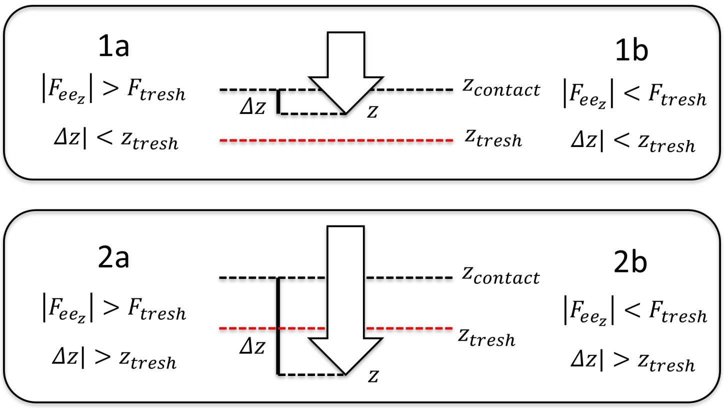
1a
$|F_{ee_z}| > F_{tresh}$
$\Delta z| < z_{tresh}$
Δz
z
$z_{contact}$
z_{tresh}
1b
$|F_{ee_z}| < F_{tresh}$
$\Delta z| < z_{tresh}$
2a
$|F_{ee_z}| > F_{tresh}$
$\Delta z| > z_{tresh}$
Δz
z
$z_{contact}$
z_{tresh}
2b
$|F_{ee_z}| < F_{tresh}$
$\Delta z| > z_{tresh}$

Figure 3.17: Scheme of the four possible contact conditions. 1a and 2a: contact happens with a material with a high Young's modulus. 1b, first phase of the contact. 2b, the material has a low Young's modulus.

As the relation involved only one axis, the gain matrix $\boldsymbol{P}$ was reduced to the constant scalar gain ρ. The logic of this additional feedback was to generate a signal that compensates the user's will, which, in this case, was an error. It is important to remember that during the operation, the end effector is situated inside the patient's body. Consequently, it is preferable to prevent impulsive behaviors by the robot. Therefore, the generated signal must be low enough to avoid the total loss of control of the robot, even for a short amount of time, but sufficiently high to provide the user with a solid constraint. In the event of an error, the user should be able to recognize it and move the robot up to a safe vertical position. In Tab 3.1, a conceptual algorithm of the switching logic, between the two profiles, is reported. In general, $\boldsymbol{\gamma_1}$ was kept as the default profile, as this profile ensured a fully compliant behavior for the robot, while $\boldsymbol{\gamma_2}$ was used only when the robot detected an error in the procedure, so when the end effector was in contact with neurovascular structures.

Algorithm 3.1 Conceptual algorithm of the switching strategy

```
No contact
$\boldsymbol{\gamma(t)} = \boldsymbol{\gamma_1(t)}$
while $|\boldsymbol{F_{ee_z}}| > 0$ (Contact detected) do
    Compute displacement from the contact point
    if $|\Delta z > z_{tresh}|$ and $|F_{ee_z}| < F_{tresh}$ (Detected contact with delicate structure) then
        $\boldsymbol{\gamma(t)} = \boldsymbol{\gamma_2(t)}$
        $\boldsymbol{z_s} = \rho \boldsymbol{F_{ee_z}}$
    else
        $\boldsymbol{\gamma(t)} = \boldsymbol{\gamma_1(t)}$
        $z_s = 0$
    end if
end while
```

Finally, in order to ensure system stability, the profile of gamma was shaped through a passivity filter. At each time instant t, its derivative $\dot{\gamma}$ was chosen as the minimum between three conditions, and then integrated to obtain the filtered γ. The details about the filter are reported in the next section.

3.3.3. Passivity analysis

In this section, the stability of the system is proved, through the passivity theory. In particular, given equation 3.17 and $\gamma(t)$ such that $0 \leq \gamma \leq 1$, the stability proof and the passivity filter developed and discussed in [20] are valid. Here, the main passages of both the proof and the theory of developing the passivity filter are reported, in the more general matrix form, for the case in which both stiffness and damping are adapted.

Consider the model of a m-joint robotic manipulator:

$$\boldsymbol{M_q(q)\ddot{q}} + \boldsymbol{C(q,\dot{q})\dot{q}} + \boldsymbol{g(q)} = \boldsymbol{\tau_c} - \boldsymbol{J(q)^T f_{ext}} \tag{3.22}$$

From section 3.3.1, in the case of impedance control, the relationship between external forces and system positions, velocities, and accelerations is the following:

$$\boldsymbol{M\ddot{e}_p} + \boldsymbol{D\dot{e}_p} + \boldsymbol{Ke_p} = \boldsymbol{f_{ext}} \tag{3.23}$$

with $\boldsymbol{e_p} = \boldsymbol{x_{ref}} - \boldsymbol{x} \in \mathbb{R}^n$, where p is the robot end-effector pose and $\boldsymbol{x_{ref}}$ a reference motion. In this discussion, the matrices $\boldsymbol{D(t)}$ and $\boldsymbol{K(t)}$ are considered time-varying, while $\boldsymbol{M}$ is assumed to be constant. From now on, time dependency will generally not be mentioned in the notations for simplicity.

In order to investigate the stability of variable impedance control given by 3.23 with varying stiffness and damping terms, first consider the following storage function:

$$\boldsymbol{V_1} = \frac{1}{2}\boldsymbol{\dot{e}_p^T M \dot{e}_p} + \frac{1}{2}\boldsymbol{e_p^T K e_p} \tag{3.24}$$

Since K and M are symmetric, differentiating V_1 leads to

$$\boldsymbol{\dot{V}_1} = \boldsymbol{\dot{e}_p^T f_{ext}} + [\frac{1}{2}\boldsymbol{e_p^T \dot{K} e_p} - \boldsymbol{\dot{e}_p^T D \dot{e}_p}] \tag{3.25}$$

If stiffness is constant or decreasing, $\boldsymbol{\dot{V}_1} \leq \boldsymbol{\dot{e}_p^T f_{ext}}$, which leads to the following passivity condition

$$\boldsymbol{V_1(t)} - \boldsymbol{V_1(0)} \leq \int_0^t \boldsymbol{\dot{e}_p^T f_{ext} d\tau} \tag{3.26}$$

With $\boldsymbol{V_1}$, passivity can only be guaranteed if the stiffness is constant or decreasing, using it as a Lyapunov function to assess stability. Since stiffness can change with respect to time, in equation 3.25 the sign of the term in brackets may change. This can cause a violation of the passivity condition 3.26 in case of increasing stiffness. For this reason, a more complicated storage function must be found. In order to facilitate the passivity analysis, consider a filtered tracking error-like variable $r \in \mathbb{R}^m$ [42] :

$$\boldsymbol{r} = \boldsymbol{\dot{e}_p} + \boldsymbol{\alpha e_p} \tag{3.27}$$

where $\alpha \in \mathbb{R}^+$ is a constant. As shown in [43], if $\boldsymbol{r}$ is bounded, then $\boldsymbol{e_p}, \boldsymbol{\dot{e}_p}$ are bounded and, in this case, if $\boldsymbol{r} \to 0$, then $\boldsymbol{e_p}, \boldsymbol{\dot{e}_p} \to 0$. So, it is possible to write:

$$\begin{aligned} \int_0^t \boldsymbol{r^T f_{ext} d\tau} &= \int_0^t \boldsymbol{r^T (M \ddot{e}_p + D \dot{e}_p + K e_p)} d\tau \\ = \int_0^t \boldsymbol{r}^T(\boldsymbol{M}(\boldsymbol{\ddot{e}_p} + \alpha \boldsymbol{\dot{e}_p}) &- \alpha \boldsymbol{M \dot{e}_p} + \boldsymbol{D \dot{e}_p} + \boldsymbol{K e_p}) d\tau \end{aligned} \tag{3.28}$$

Using equation 3.27 and its derivative it follows that

$$\int_0^t (\boldsymbol{r^T f_{ext}} d\tau = \int_0^t \boldsymbol{r^T M \dot{r}} + \boldsymbol{\dot{e}_p^T}(\boldsymbol{D} - \alpha \boldsymbol{M})\boldsymbol{\dot{e}_p} + \boldsymbol{e_p^T}(\boldsymbol{K} + \alpha \boldsymbol{D} - \alpha^2 \boldsymbol{M})\boldsymbol{\dot{e}_p} + \boldsymbol{e_P^T}(\alpha \boldsymbol{K})\boldsymbol{e_p}) d\tau \tag{3.29}$$

By introducing a symmetric, positive semidefinite, and continuously differentiable matrix $\boldsymbol{C_s}$, equation 3.29 can be written as:

$$\begin{aligned} \int_0^t \boldsymbol{r^T f_{ext}} d\tau = \int_0^t (\boldsymbol{r^T M \dot{r}} + \boldsymbol{e_p^T C_s \dot{e}_p^T} + \frac{1}{2}\boldsymbol{e_p^T \dot{C}_s e_p}) d\tau + \\ + \int_0^t (\boldsymbol{\dot{e}_p^T}(\boldsymbol{D} - \alpha_s \boldsymbol{M})\boldsymbol{\dot{e}_p} + \boldsymbol{e_p^T}(\alpha_s \boldsymbol{K} - \frac{1}{2}\boldsymbol{\dot{C}_s e_p} + \boldsymbol{e_p^T}(\boldsymbol{K} + \alpha_s \boldsymbol{D} - \alpha_s^2 \boldsymbol{M} - \boldsymbol{C_s})\boldsymbol{\dot{e}_p})) d\tau \end{aligned} \tag{3.30}$$

which can be written as

$$\int_0^t \boldsymbol{r^T f_{ext}} d\tau = \boldsymbol{V_2(t)} - \boldsymbol{V_2(0)} + \int_{\boldsymbol{0}}^{\boldsymbol{t}} \boldsymbol{W_2 d}\tau \tag{3.31}$$

with

$$\boldsymbol{V_2} = \frac{1}{2}\boldsymbol{r^T M r} + \frac{1}{2}\boldsymbol{e_p^T C_s e_p} \tag{3.32}$$

and

$$\boldsymbol{W_2} = \boldsymbol{\dot{e}_p^T}(\boldsymbol{D} - \alpha_s \boldsymbol{M})\boldsymbol{\dot{e}_p} + \boldsymbol{e_p^T}(\alpha_s \boldsymbol{K} - \frac{1}{2}\boldsymbol{\dot{C}_s e_p} + \boldsymbol{e_p^T}(\boldsymbol{K} + \alpha_s \boldsymbol{D} - \alpha_s^2 \boldsymbol{M} - \boldsymbol{C_s})\boldsymbol{\dot{e}_p}) \tag{3.33}$$

As reported in [20], by defining $\boldsymbol{C_s} = \boldsymbol{K} + \alpha_s \boldsymbol{D} - \alpha_s^2 \boldsymbol{M}$, the candidate storage function 3.32 results in the stability conditions:

$$0 \leq \boldsymbol{D} - \alpha_s \boldsymbol{M} \tag{3.34}$$

$$0 \leq 2\alpha_s\boldsymbol{K} - \dot{\boldsymbol{K}} - \alpha_s\dot{\boldsymbol{D}} \tag{3.35}$$

This choice leads to $\boldsymbol{W_2} \geq 0$, which allows to conclude on system passivity, by the fact that equation 3.31 leads to

$$\boldsymbol{V_2(t)} - \boldsymbol{V_2(0)} \leq \int_0^t \boldsymbol{r^T f_{ext}} d\tau \tag{3.36}$$

The main limitation of this analysis is that, given a generic variable impedance profile, passivity conditions 3.34 and 3.35 can be used only to verify whether passivity is guaranteed. A method to change this profile, in order to ensure passivity in every time instant, is explored.

Consider the change in system impedance, with in general the stiffness and the damping varying from $\boldsymbol{K_0}$ to $\boldsymbol{K_1}$ and from $\boldsymbol{D_0}$ to $\boldsymbol{D_1}$ respectively. Here, only the case $\boldsymbol{K_0} < \boldsymbol{K_1}$ is reported. Now consider the following profiles for $\boldsymbol{K}$ and $\boldsymbol{D}$:

$$\boldsymbol{K} = \boldsymbol{K(t)} = \boldsymbol{K_0} + \boldsymbol{\Gamma(t)\delta K} \tag{3.37}$$

$$\boldsymbol{D} = \boldsymbol{D(t)} = \boldsymbol{D_0} + \boldsymbol{\Gamma(t)\delta D} \tag{3.38}$$

with $\boldsymbol{\delta K} = \boldsymbol{K_1} - \boldsymbol{K_0}$, $\boldsymbol{\delta D} = \boldsymbol{D_1} - \boldsymbol{D_0}$, and $\boldsymbol{\Gamma}$ a diagonal matrix where all diagonal terms $\boldsymbol{\gamma_i}$ are differentiable gains such that $0 \leq \boldsymbol{\gamma_i} \leq 1$. Since $\boldsymbol{M}$, $\boldsymbol{K}$, $\boldsymbol{D}$ were chosen to be diagonal, the impedance behavior can be decoupled. In order to ensure passivity using conditions on V_2, K and D need to satisfy equations 3.34 and 3.35. Condition 3.34 allows choosing α easily. Condition 3.35 implies that $\forall i \in 1, 2, ..., n$

$$\dot{\gamma}_i(\alpha_s\delta d_i + \delta k_i) - 2\alpha_s(k_{0_i} + \gamma\delta k_i) \leq 0, \tag{3.39}$$

with δk_0 and δd_0 the diagonal terms of $\boldsymbol{\delta K}$ and $\boldsymbol{\delta D}$ respectively, and k_{0_i} the diagonal terms of K_0. Assume that $\delta d_i \geq 0$. As $\delta k_i > 0$ and $\alpha_s \geq 0$, then $\alpha_s\delta d_i + \delta k_i > 0$. Condition 3.39 can be rewritten as

$$\dot{\boldsymbol{\gamma}}_{\boldsymbol{i}} \leq a_i\boldsymbol{\gamma_i} + b_i, \tag{3.40}$$

with

$$a_i = \frac{2\alpha\delta k_i}{\alpha\delta d_i + \delta k_i}, b_i = \frac{2\alpha k_{0_i}}{\alpha\delta d_i + \delta k_i} \tag{3.41}$$

Combining equation 3.39 with a low-pass filter, in order to ensure smoothness of γ_i, a passivity filter can be designed in such a way that it takes as input the desired switching profile $\bar{\gamma}_i$ and generates an output profile γ_i that guarantees the system passivity. The filter, as reported in the cited study, is defined by

$$\dot{\boldsymbol{\gamma}}_{\boldsymbol{i}} = min(\beta(\bar{\boldsymbol{\gamma}}_{\boldsymbol{i}} - \boldsymbol{\gamma}_{\boldsymbol{i}}), a_i\boldsymbol{\gamma}_{\boldsymbol{i}} + b_i) \tag{3.42}$$

where β is the filter parameter. By integrating 3.42 it is possible to obtain $\boldsymbol{\gamma}_{\boldsymbol{i}}$ that tracks $\bar{\gamma}_i$ in such a way that passivity conditions are respected. Again, in [20], less conservative passivity conditions are searched, in order to obtain a better tracking performance..

To do so, the assumptions on 3.27 are modified, to replace α_s by a time-dependent diagonal matrix B_s with bounded eigenvalues:

$$r = \dot{e}_p + M^{-1}B_s e_p \tag{3.43}$$

Considering 3.43 with M constant diagonal matrix and B_s a time-dependent diagonal matrix with bounded eigenvalues. In this case, using the same strategy as before yelds to:

$$\int_0^t \boldsymbol{r^T f_{ext}} d\tau = \boldsymbol{V_3(t)} - \boldsymbol{V(0)} + \int_0^t \boldsymbol{W_3} d\tau \tag{3.44}$$

with

$$\boldsymbol{V_3} = \frac{1}{2}\begin{bmatrix}\dot{\boldsymbol{e}}_{\boldsymbol{p}} \\ \boldsymbol{e_p}\end{bmatrix}^T \begin{bmatrix}\boldsymbol{M} & \boldsymbol{B_s} \\ \boldsymbol{B_s} & \boldsymbol{C_s} + \boldsymbol{B_s M^{-1} B_s}\end{bmatrix}\begin{bmatrix}\dot{\boldsymbol{e}}_p \\ \boldsymbol{e_p}\end{bmatrix} \tag{3.45}$$

and

$$\begin{aligned}\boldsymbol{W_3} = \dot{\boldsymbol{e}}_{\boldsymbol{p}}^{\boldsymbol{T}}(\boldsymbol{D} - \boldsymbol{B_s})\dot{\boldsymbol{e}}_{\boldsymbol{p}} + \boldsymbol{e_p^T}(\boldsymbol{B_s M^{-1}}(\boldsymbol{K} - \dot{\boldsymbol{B}}_s) - \boldsymbol{\frac{1}{2}}\dot{\boldsymbol{C}}_s)\boldsymbol{e_p} + \\ + \boldsymbol{e_p^T}(\boldsymbol{K} - \boldsymbol{B_s M^{-1}}(\boldsymbol{D} - \boldsymbol{B_s}) - \dot{\boldsymbol{B}}_s - \boldsymbol{C_s})\dot{\boldsymbol{e}}_{\boldsymbol{p}}\end{aligned} \tag{3.46}$$

The choice $\boldsymbol{C_s} = \boldsymbol{K} + \boldsymbol{B_s M^{-1}(D - B_s)} - \dot{\boldsymbol{B}}_{\boldsymbol{s}}$ allows canceling out the cross-terms. Considering 3.46, the positivity of $\boldsymbol{V_3}$ is obtained if $0 \leq \boldsymbol{C_s}$

The positivity of W_3 is obtained if the following passivity conditions hold

$$
\begin{aligned}
&0 \leq \boldsymbol{D} - \boldsymbol{B_s} \\
&0 \leq \boldsymbol{B_s M^{-1}(K} - \dot{\boldsymbol{B}}_{\boldsymbol{s}}\boldsymbol{)} - \frac{1}{2}\dot{\boldsymbol{C}}_{\boldsymbol{s}}
\end{aligned}
\tag{3.47}
$$

Choosing $\boldsymbol{B_s} = \boldsymbol{D}$, $\boldsymbol{C} = \boldsymbol{K} - \dot{\boldsymbol{D}}$, a fourth storage function is then defined:

$$
\boldsymbol{V_4} = \frac{1}{2}\begin{bmatrix} \dot{\boldsymbol{e}}_{\boldsymbol{p}} \\ e_p \end{bmatrix}^T \begin{bmatrix} \boldsymbol{M} & \boldsymbol{D} \\ \boldsymbol{D} & \boldsymbol{K} + \boldsymbol{DM^{-1}D} - \dot{\boldsymbol{D}} \end{bmatrix} \begin{bmatrix} \dot{\boldsymbol{e}}_{\boldsymbol{p}}\boldsymbol{e_p} \end{bmatrix}
\tag{3.48}
$$

and the resulting passivity conditions are obtained:

$$
\begin{aligned}
&0 \leq \boldsymbol{K} - \dot{\boldsymbol{D}} \\
&0 \leq 2\boldsymbol{DM^{-1}(K} - \dot{\boldsymbol{D}}\boldsymbol{)} - \dot{\boldsymbol{K}} + \ddot{\boldsymbol{D}}
\end{aligned}
\tag{3.49}
$$

As previously, all matrices are chosen diagonal and the problem can be decoupled, thus 3.49 is equivalent to:

$$
\dot{k}_i + \frac{2}{m_i}d_i\dot{d}_i - \ddot{d}_i - \frac{2}{m_i}k_i d_i \leq 0
\tag{3.50}
$$

resulting in

$$
-a_{1i}\ddot{\boldsymbol{\gamma}}_{\boldsymbol{i}} + a_{2i}\dot{\boldsymbol{\gamma}}_{\boldsymbol{i}} + a_{3i}\boldsymbol{\gamma_i}\dot{\boldsymbol{\gamma}}_{\boldsymbol{i}} - a_{4i}\boldsymbol{\gamma_i} - a_{5i}\boldsymbol{\gamma_i}^2 - a_{6i} \leq 0
\tag{3.51}
$$

with

$$
\begin{aligned}
&a_{1i} = \delta d_i \qquad && a_{2i} = \delta k_i + \frac{2}{m_i}d_{0i}\delta d_i \\
&a_{3i} = \frac{2}{m_i}\delta d_i^2 \qquad && a_{4i} = \frac{2}{m_i}(d_{0i}\delta k_i + k_{0i}\delta d_i) \\
&a_{5i} = \frac{2}{m_i}\delta k_i \delta d_i \qquad && a_{6i} = \frac{2}{m_i}k_{0i}d_{0i}
\end{aligned}
\tag{3.52}
$$

wich are all positive since $\delta\boldsymbol{K}$ and $\delta\boldsymbol{D}$ are positive. For pratical implementation, the term

$-a_{1i}\ddot{\gamma}_i$ is not considered in writing the final condition on $\dot{\gamma}_i$, because computing $\ddot{\gamma}_i$ can be problematic, since $\dot{\gamma}_i$ can be discontinuous. Therefore, the following conditions are used:

$$\begin{aligned} \dot{\gamma}_i \leq \frac{\delta k_i}{\delta d_i}\gamma_i + \frac{k_{0i}}{\delta d_i} \triangleq h_{1i} \\ \dot{\gamma}_i \leq \frac{a_{4i}\gamma_i + a_{5i}\gamma_i^2 + a_{6i}}{a_{2i} + a_{3i}\gamma_i} \triangleq h_{2i} \end{aligned} \tag{3.53}$$

The passivity filter is therefore obtained as:

$$\dot{\gamma}_i = min(h_{1i}(\gamma_i), h_{2i}(\gamma_i), \beta(\overline{\gamma}_i - \gamma_i)) \tag{3.54}$$

3.4. Experimental setup

In this section, the experimental setup is described. First, a technical characterization was performed to evaluate the system's performance in terms of the control strategy. Finally, a user study was performed to determine whether the proposed system could reduce the risk of damaging delicate materials, with respect to a constant impedance hands-on control.

3.4.1. System validation

A technical validation was performed to inspect the behavior of the overall control system. First, the stability of the control scheme was tested. The task involved the user wearing the MyoWristband on their forearm and using it to guide the robot end-effector against a given material while applying a constant force and maintaining contact with the material. The z position of the end effector (refer to Figure 3.6 in previous section) was recorded to investigate the presence of oscillations and thus the stability of the system. In particular, it was expected that, in the first phase of contact, the z position decreased until $z_{curr} > z_{tresh}$. Then, an equilibrium position is expected to be reached as long as contact was kept with the material: the end effector position should remain almost constant, with no significant oscillations. Then, in order to assess system reliability and test the correct behavior of the control law, 10 repetitions of the same task were performed on different materials. Four materials were chosen (Figure 3.18), based on the mechanical characterization discussed in Section 2.1: a polyurethane sponge with a Young modulus of $\approx 1 - 5MPa$, foam rubber with a Young modulus of $\approx 10 - 15MPa$, a polyvinyl acetate (PVA) sponge with a Young modulus of $\approx 20 - 30MPa$ and a polylactic acid (PLA) vertebra phantom, with a Young modulus of $\approx 5 - 10GPa$.

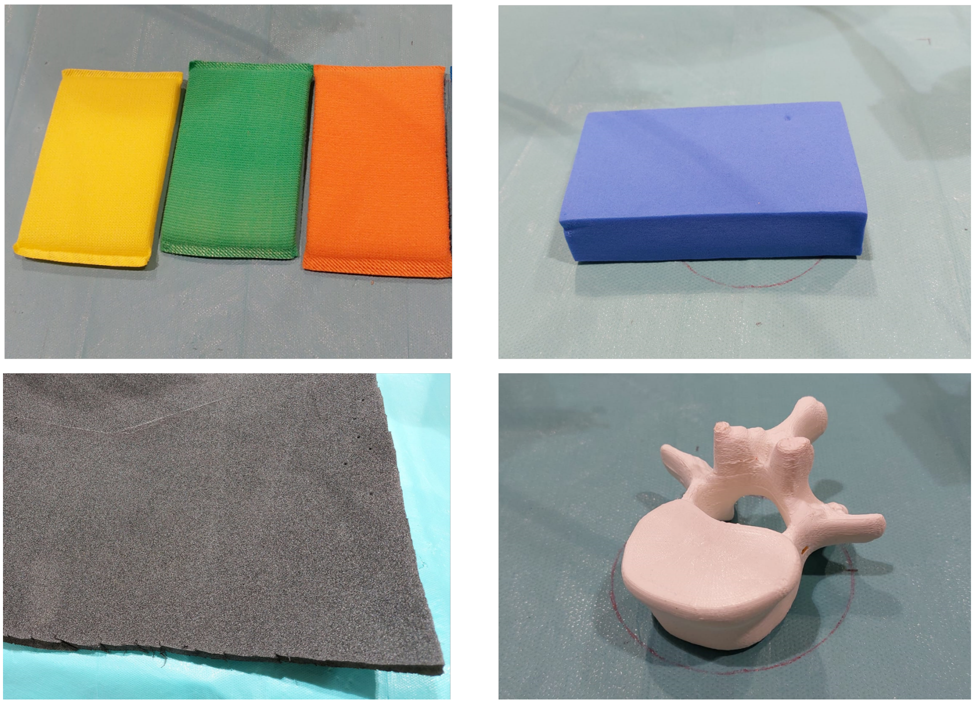

Figure 3.18: Chosen materials: polyurethane sponges (upper left), foam rubber (down left), PVA sponge (upper right), PLA vertebra phantom (down right).

The goal was to demonstrate that the strategy guaranteed an increasing profile for the adaptive stiffness $\boldsymbol{k_z(t)}$ when contact was made with a material with low Young's modulus and that a low value was reached otherwise. Moreover, to validate the behavior of the safety feedback, the profile of $\boldsymbol{z_s(t)}$ must be analyzed, which is expected to increase in the range $[0, 0.05]\, m$ for the first three materials. To assess this analysis, the average values of stiffness $\hat{k}_z$ and position correction $\hat{z}_c$ on the 10 repetitions were computed.

3.4.2. User Study

A User Study has been performed, to compare the performance of a constant impedance hands-on control (Mode 1) with the proposed control strategy (Mode 2). The goal was to demonstrate that the proposed strategy prevented the users from damaging delicate materials while allowing them to operate on a bone-like material. In these experiments, three different materials have been used: the polyurethane sponge, the PVA sponge, and the PLA vertebra phantom. They were placed inside a box, such that the user did not have visual feedback on the contact surface. Users were instructed to guide the robot through the object, apply a force as if attempting to perforate the material and maintain contact for around 5 seconds. For each material, the task was repeated three times. Data have been collected from 10 different users, with 3 repetitions for each material and all users gave their informed consent before participating in the study. To validate the research hypothesis, the contact force, $\boldsymbol{F}_{\boldsymbol{ee_z}}$, between the robot end effector and the materials and the displacement z_d were analyzed. The displacement (Figure 3.19) was computed from the contact point, $z_{contact}$, between the end-effector and the material, to the minimum point reached by the tooltip, z_{min}:

$$z_d = z_{contact} - z_{min}$$

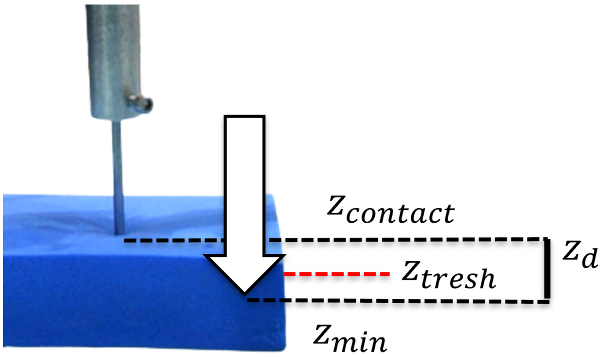

Figure 3.19: z_d is computed from the contact point $z_{contact}$ to the minimum z position that the tooltip reaches z_{min}.

The average values $\hat{F}_{ee_z}$ and $\hat{z}_d$ were computed for each material $m \in [1, 2, 3]$, according to the following equations:

$$\hat{F}^m_{ee_z} = \frac{\sum_{i=1}^{r} \boldsymbol{F}^{\boldsymbol{i}}_{\boldsymbol{ee_z}}}{r} \tag{3.1}$$

$$\hat{z}^m_d = \frac{\sum_{i=1}^{r} |z^i_d|}{r} \tag{3.2}$$

where $r = 3$ are the repetitions for each user. A lower contact force $\boldsymbol{F}_{\boldsymbol{ee_z}}$ and a lower displacement z_d were expected in case of contact with materials with low Young's modulus when using the proposed strategy. In the case of contact with materials with high Young's modulus, a similar performance between Mode 1 and Mode 2 was expected. In order to assess the statistical validity of the collected data distributions, the Wilcoxon ranksum test was performed. In fig 3.20 and 3.21, the experimental setup is depicted.

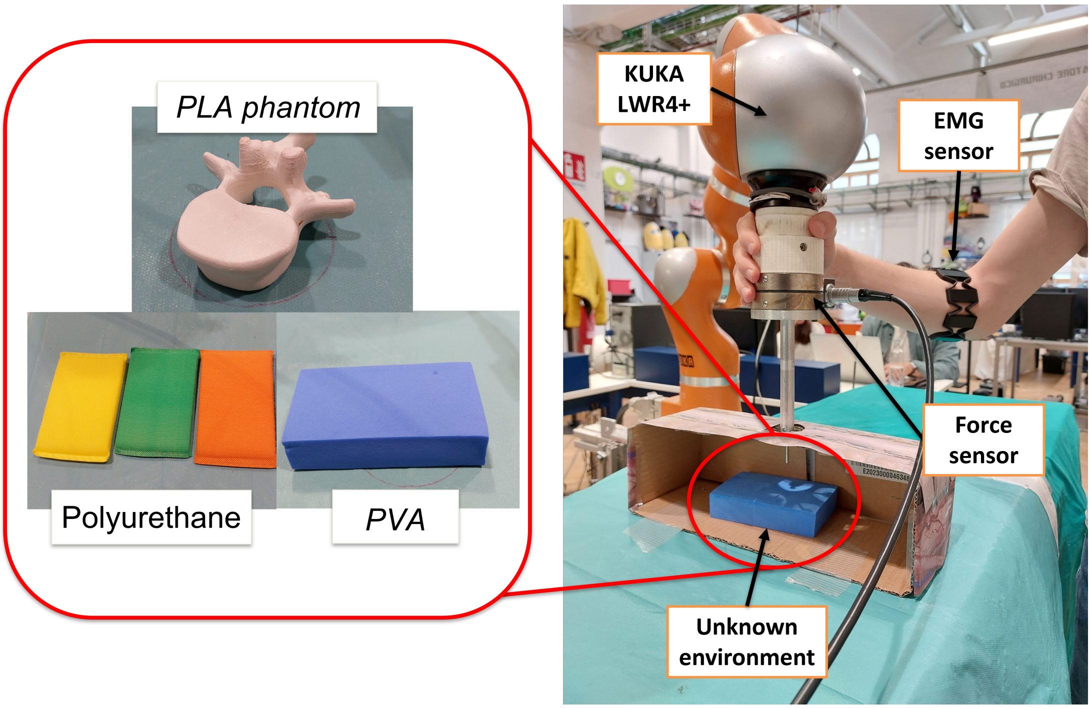
PLA phantom
Polyurethane
PVA
KUKA LWR4+
EMG sensor
Force sensor
Unknown environment

Figure 3.20: Experimental setup in the User Study. The user guides the robot, equipped with the force sensor against different materials, placed inside a box. In Mode 2, the user is also wearing the MyoWristband on the forearm.

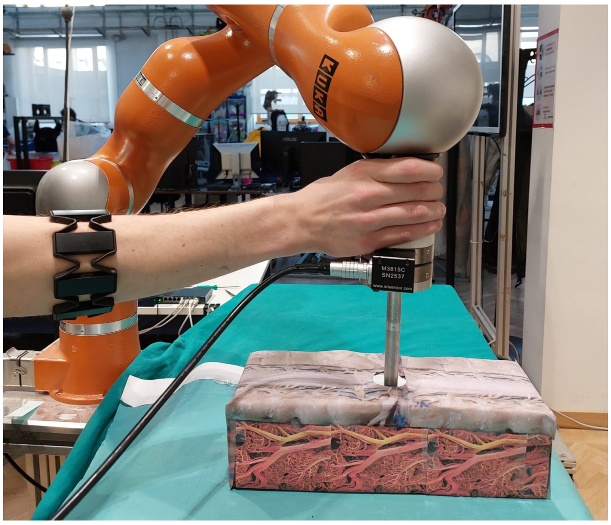

Figure 3.21: Experimental setup in the User Study: user perspective.

Finally, a qualitative analysis was proposed. After the repetitions, each user was asked to fill out a form, in order to obtain a qualitative analysis of the performance of the system. In particular, they were asked to express their level of agreement with eight statements, on a scale from 1 (totally disagree) to 5 (totally agree). Here are reported the eight statements, proposed for both Mode 1 and Mode 2:

User study questionnaire	
S1	The system was easy to use
S2	People can learn to use this system very easily
S3	It is required a priori knowledge in order to use this system
S4	The system was subjected to inconsistency among repetitions
S5	It was easy to damage the material
S6	I was able to distinguish easily the different materials, despite I had no visual feedback
S7	With some materials, the robot was not allowing me to complete the task
S8	The task was mentally demanding

Table 3.3: For both tasks, users were asked to express their level of agreement with each of the 8 statements reported

3.4.3. Choice of control parameters

The experiments were performed using the LWR4+ (KUKA) as the robotic manipulator and the MyoWristband for the EMG acquisition. The main impedance controller and the adaptive law were written in C++ and they communicated with the FRI at 100 Hz, using ROS. The sensor force and EMG processed data were acquired at 50 Hz. For both experiments, the following values for the parameters were adopted. In particular, regarding the impedance controller and the adaptive law, a range of $\boldsymbol{k_z}$ between $k_0 = 100N/m$ and $k_1 = 1000N/m$ was considered. Full compliantness can be obtained with $\boldsymbol{k_z} \approx 0$, but unfortunately, this choice could cause torque errors, related to the internal decoupled motor controllers, especially on the orientation. For this reason, the lower bound on the z-axis k_0 was set to 100. Since the strategy was focused on the z-axis, the stiffness component of the other axes was kept constant, more precisely, $k_x = k_y = 100N/m$, $k_{rx} = k_{ry} = k_{rz} = 300N/m$. The choice of the orientation parameters was due to the fact that, during the repetitions of the tasks, the orientation of the end-effector should remain constant. Regarding the damping parameters, while a low damping ratio typically results in a more compliant manipulator, in the context of spinal surgery, a damping ratio of 0.8 may be more appropriate to improve precision. Moreover, unlike in industrial applications, high-velocity behaviors are not necessary for this context. For this reason, this value was kept constant: $d_i = 0.8 \ \forall i \in [x, y, z, rx, ry, rz]$. Finally, a weight $\alpha = 0.1$ was chosen, as a result of a compromise between the two performances required: γ_1 low at high contact forces and γ_2 high at low contact forces. Regarding the switching logic, a force threshold of $F_{tresh} = 15 \ N$ was chosen, as a result of empirical considerations on different materials. As displacement treshold, $z_{treshold} = 0.005\ m$ was chosen. A smaller threshold would have been irrealistic, due to the fact that in a real scenario, the patient will not remain perfectly still, due to breathing and other complications that can cause errors in the position measurement of the tooltip [44]. A bigger threshold however could generate an overall unsafe procedure, caused by the unwanted drilling of the tissue before the activation of the strategy. Considering the position correction generation, a constant $\rho = 0.004\ m/N$ was chosen, based on empirical considerations. In this way, the z_s generated was in the range of centimeters, which was considered enough to increase the safety of the operation, but also as small as needed to not generate unwanted behaviors on the robot. It is important to remember that, as the end-effector proceeds with the operation, the tip is located inside the patient's body. Finally, for the User Study, the stiffness of the constant impedance controller was set to $k_{z_c} = 500\ N/m$.

The values of the parameters are summarized in Tab (3.4).

Control logic parameters	
k_0	100 [N/m]
k_1	1000 [N/m]
d_i	0.8
α	0.1
$z_{treshold}$	0.005 [m]
$F_{treshold}$	15 [N]
ρ	0.004 [m/N]
k_{z_c}	500 [N/m]

Table 3.4: Values of the parameters selected for the control strategy

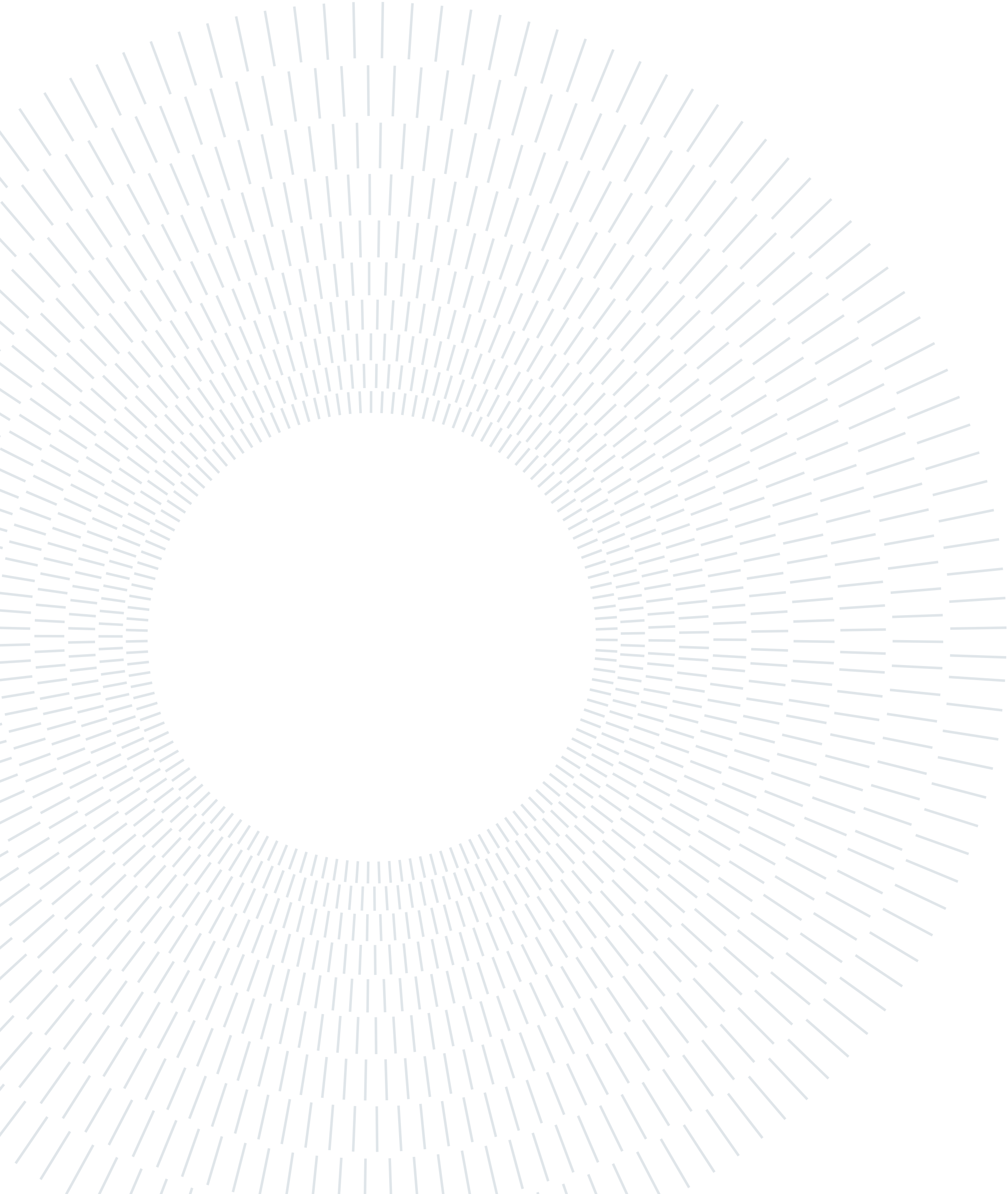

4 | Results

4.1. Force sensor

The MultiLayer Perceptron Regressor model was evaluated using the mean square error (MSE) and the R^2 score. The performance of the network is represented by an R^2 score of 0.96 and an MSE of 0.006, demonstrating its ability to accurately predict the force read by the force sensor after removing the tool's gravity contribution, regardless of the end-effector orientation. In Figure 4.1, the comparison between the predicted and true values is shown.

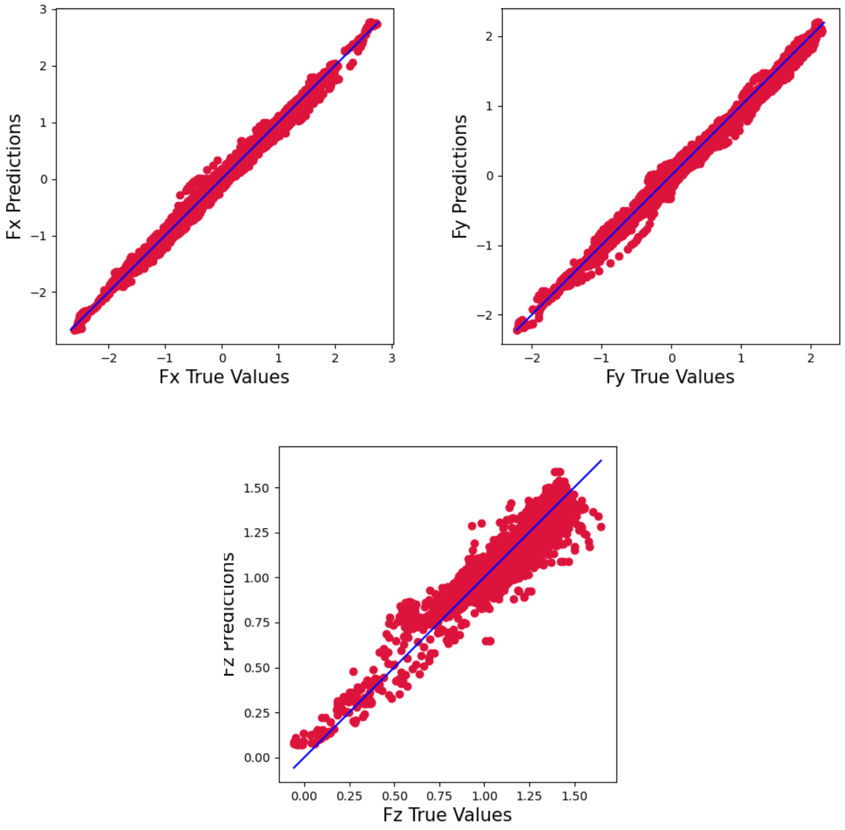

Figure 4.1: Validation of the force sensor tool weight compensation. In red, true force values are represented, while in blue the force predicted by the MLP is shown.

4.2. Human force estimation

The LSTM model has been validated with the remaining 20% of the data. The network was evaluated using the mean square error (MSE) and the R^2 score. The performance of the network is represented by an R^2 score of 0.558 and an MSE of 0.01. In Figure 4.2 the validation loss function is shown. These results suggest that the quality of the signal produced from the trained network is low. Some improvements may be obtained by including, in the input data, robots joint-specific information, such as position and speed, or by considering alternative EMG sensors.

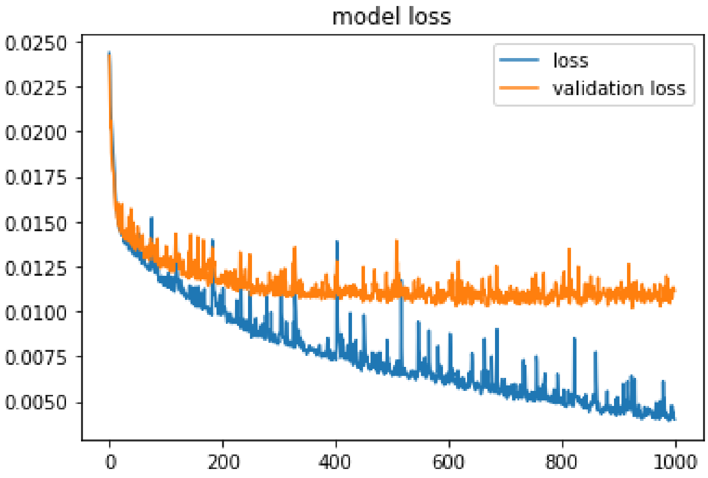

Figure 4.2: Loss function of training and validation dataset

In Figure 4.3, a plot of the human estimated force is shown. When the user applies a force on the robot and moves it, high peaks are obtained. When the user removes the hand from the robot and keeps it at rest, a low force value is obtained.

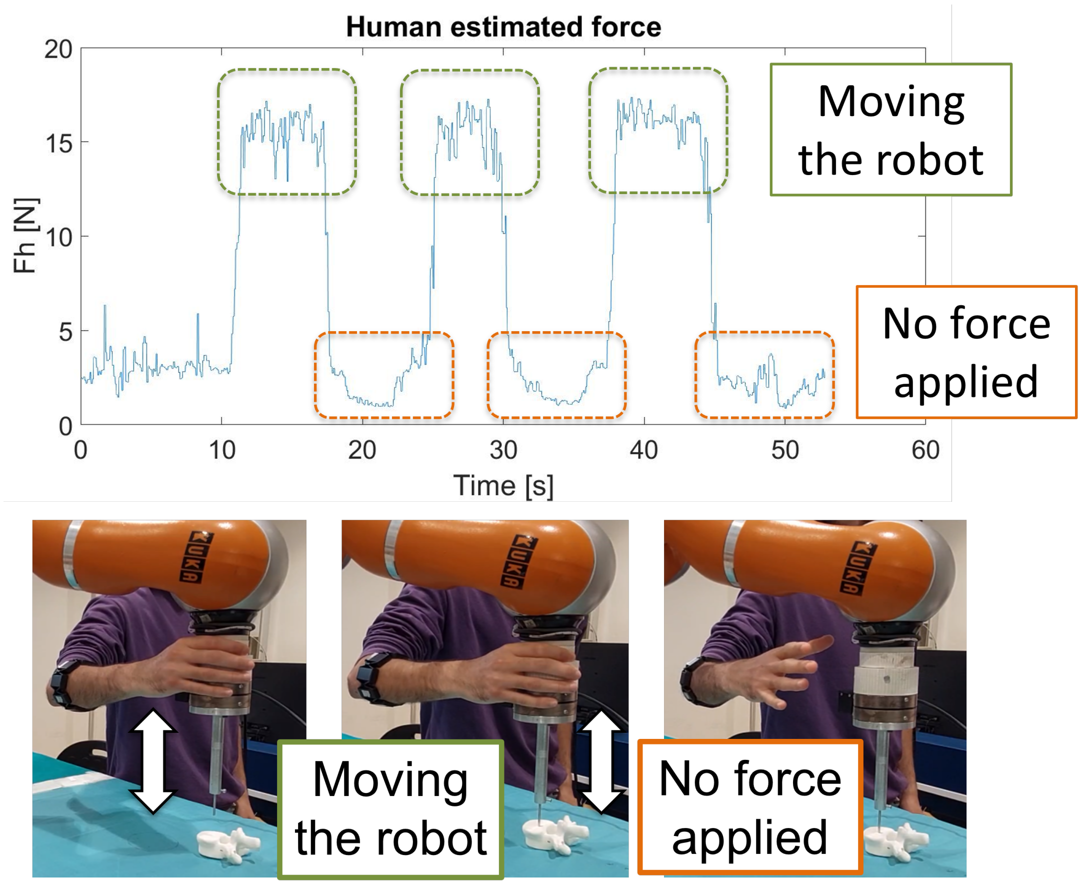

Figure 4.3: Human force estimated online with the LSTM trained model. Depending on the muscle activity of the user, the predicted force changes between high and low values.

4.3. Validation of control scheme

In the following section, the results of the validation experiment are reported. First, the stability of the system is inspected by considering one repetition of the task described in Chapter 3 and by looking at the measured position on the end effector $\boldsymbol{z_{curr}}$ when contact is made. In Figure 4.4, the end effector z position is shown, with respect to time. For completeness, the corresponding plots of the measured force, stiffness $\boldsymbol{k_z}$, and additional position feedback $\boldsymbol{z_s}$ are also reported.

In the first 4 seconds, the user is guiding the robot along the z-axis, toward the material. At 4 seconds, contact with the material is made. When the displacement becomes higher than z_{tresh}, the safety feedback is generated and the end effector position stabilizes around an equilibrium point without oscillations. At 14s, the user starts moving the robot back to the initial position.

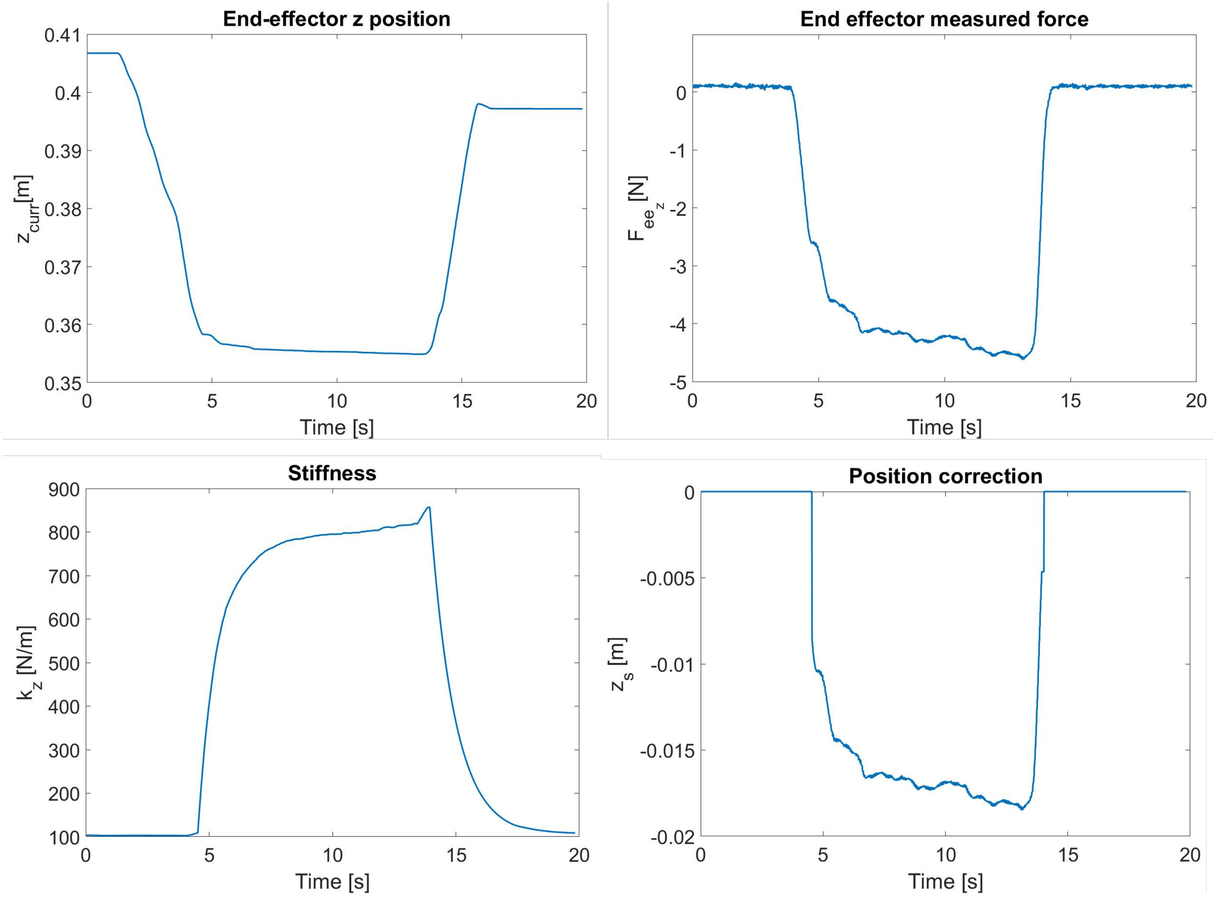

Figure 4.4: Upper left: end effector z position, $\boldsymbol{z_{curr}}$. Upper right: contact force, $\boldsymbol{F_{ee_z}}$. Down left: robot stiffness, $\boldsymbol{k_z}$. Down right: position feedback, $\boldsymbol{z_s}$. Contact with polyurethane.

After the stability analysis, the validation of the adaptive stiffness, $\boldsymbol{k_z}$, of the robot and the generated position correction, $\boldsymbol{z_s}$, was performed. In fig 4.5 and 4.6, the boxplot of the adaptive stiffness of the robot and the generated position correction of the 10 repetitions is reported, for each material. An increasing stiffness profile, $\boldsymbol{k_z}$, can be seen in the first three materials, with an average value of $658.28 \pm 221.09\, N/m$ for polyurethane, $624.75 \pm 227.9\, N/m$ for the foam rubber, and $397.5 \pm 195.85\, N/m$ for the PVA. The value recorded in the PVA material is smaller than the one obtained in the other two materials but it is compensated by a higher position correction, which reaches an average value of $0.0339 \pm 0.01\, m$. For polyurethane and for foam rubber, an average value of the generated position correction, z_s, of $0.0182 \pm 0.0053\, m$ and $0.0267 \pm 0.0083\, m$ was recorded, respectively. Moreover, high values in the standard deviation of the stiffness can be observed but it can be justified by the fact that, at the beginning of each repetition, the stiffness value is always very low. Considering the PLA vertebra, even though it was not possible to drill it because of the limitations of the setup, the stiffness keeps a low value: $\hat{k}_z = 140.85 \pm 14.88\, N/m$ with a low standard deviation. The test showed that, when contact happens with materials that deform if subjected to low forces, the strategy guaranteed an increasing stiffness, $\boldsymbol{k_z}$, and the generation of a safety command, $\boldsymbol{z_s}$, both inside the defined ranges.

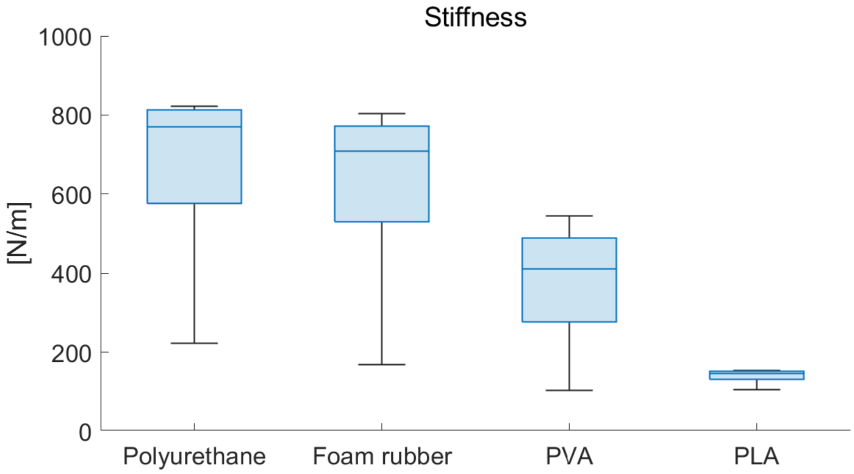

Figure 4.5: Validation experiments: comparison of the boxplots of the stiffness $\boldsymbol{k_z}$ for all the materials

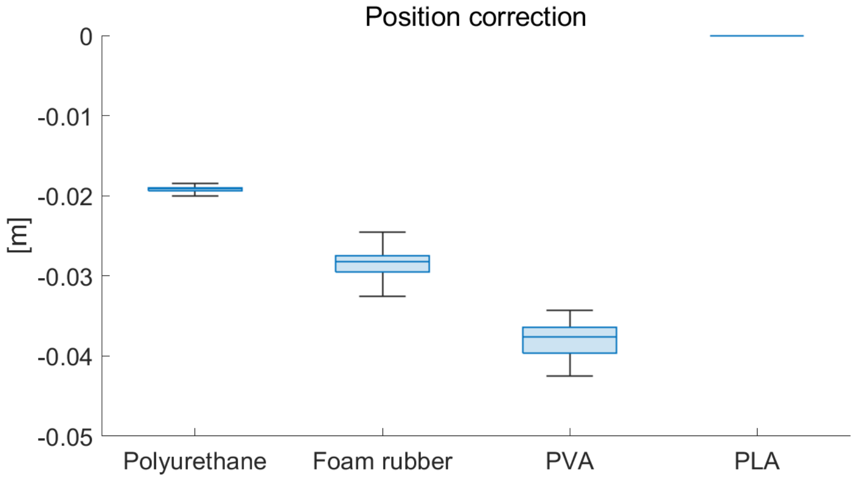

Figure 4.6: Validation experiments: comparison of the boxplots of the safety position correction $\boldsymbol{z_s}$ for all the materials

4.4. User study

For each material, the average force and displacement among the 10 users were computed for each modality. The Wilcoxon ranksum test was used to compare the two modalities with a statistical significance assessed at 0.05. In Figure 4.7 and 4.8 the corresponding boxplots for each material are shown. The average displacement was found significantly lower (p-value < 0.05) in Material 1 with a mean value of $0.0074 \pm 0.0018\ m$ and $0.019 \pm 0.0068\ m$ for Mode 2 and Mode 1, respectively. Also for Material 2, a significant difference was found (p-value < 0.05) when comparing Mode 2 with Mode 1 with an average displacement of $0.0079 \pm 0.0027\ m$ and $0.0171 \pm 0.003\ m$ respectively. The results in terms of displacement show that the proposed strategy is able to recognize the type of material and prevent the user from guiding the robot through it. Furthermore, a significant difference was found in the force measured on the end-effector between Mode 1 and Mode 2 for both Material 1 and Material 2. In Material 1, Mode 2 resulted in an average force of $-5.065 \pm 1.45\ N$, which was significantly lower than the average force of $-13.72 \pm 6.52\ N$ measured in Mode 1. Similarly, for Material 2, Mode 2 had an average force of $-5.65 \pm 2.57\ N$, which was significantly lower than the average force of $-14.79 \pm 5.15\ N$ measured in Mode 1. The lower measured force in Mode 2 when compared to Mode 1 shows that the system is able to reduce the contact force between the tooltip and the material. In this way, the risk of the material being damaged is successfully reduced. The results for Material 3 were not statistically significant, with a p-value > 0.05 for both displacement and force. This was expected since Material 3 has a high Young's modulus, and the proposed strategy was designed to keep the robot compliant during contact with such materials. Therefore, the results of the study successfully demonstrated that the proposed strategy was effective in preventing damage to delicate materials while still allowing for effective manipulation of materials with a high Young's modulus.

.

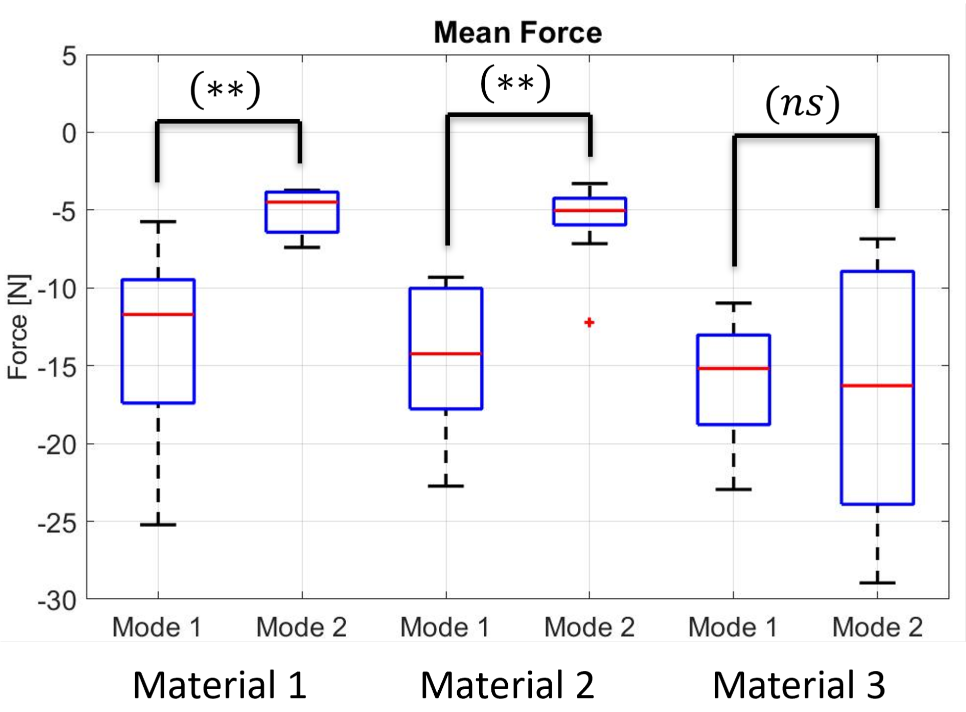

Figure 4.7: Boxplots of the mean force $\hat{F}_{ee_z}$ for each material

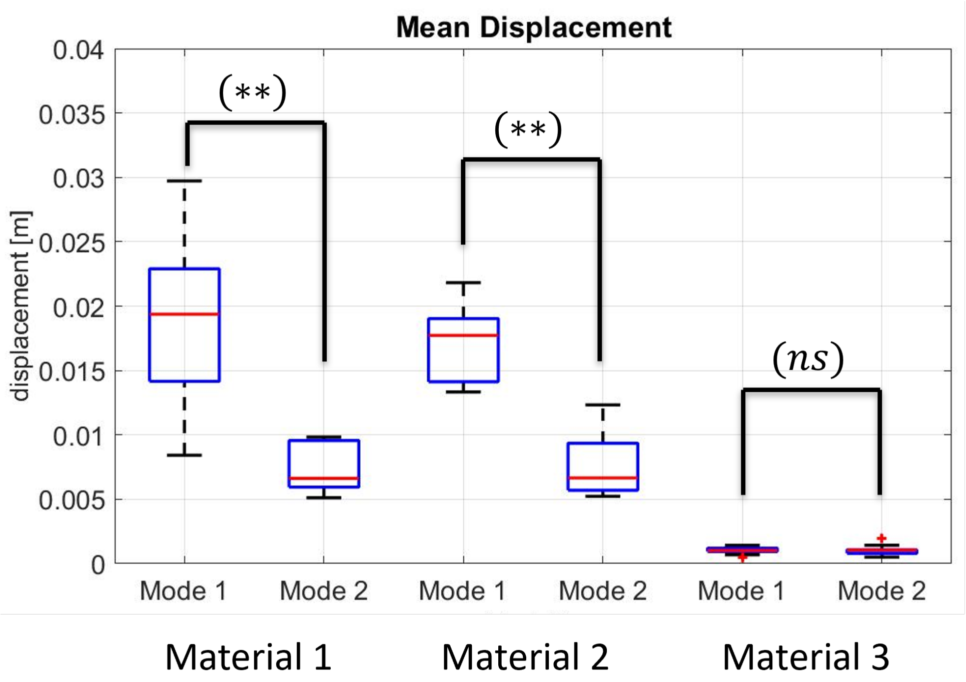

Figure 4.8: Boxplots of the mean displacement $\hat{z}_s$ for each material

The comparison of the stiffness profile $\boldsymbol{k_z}$ and the position feedback $\boldsymbol{z_s}$ between the two

modalities is meaningless, however, the average and standard deviations obtained in Mode 2, for all materials, are reported for completeness. For material 1 an average stiffness of $641.94 \pm 232.97\, N/m$ and an average safety feedback of $-0.015 \pm 0.0062\, m$, were recorded. For material 2 the average stiffness was $662.66 \pm 223.35\, N/m$, with an average safety feedback of $-0.016 \pm 0.0077\, m$. The high values of the stiffness standard deviations are justified by the fact that, at the beginning of each repetition, the stiffness value was always very low. For material 3, the average stiffness was successfully kept low, equal to $141.27 \pm 25.34\, N/m$, and no safety feedback was generated.
In Figure 4.9 and 4.10 the stiffness and safety feedback profiles obtained from one user in Mode 2, for all materials, are reported.

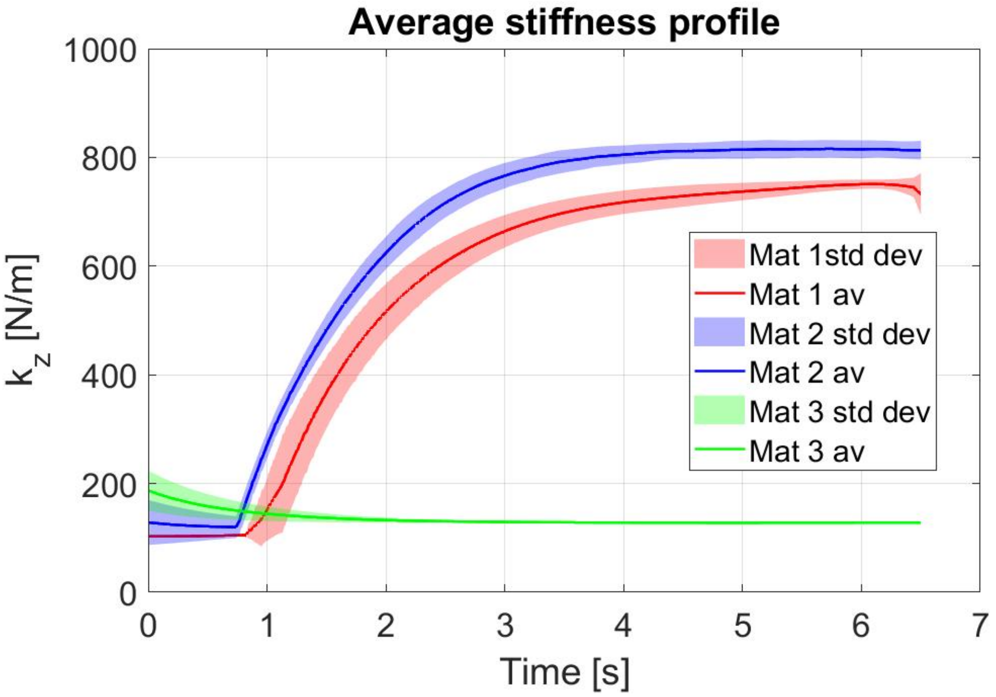

Figure 4.9: Stiffness profile $\boldsymbol{k_z}$ for all materials

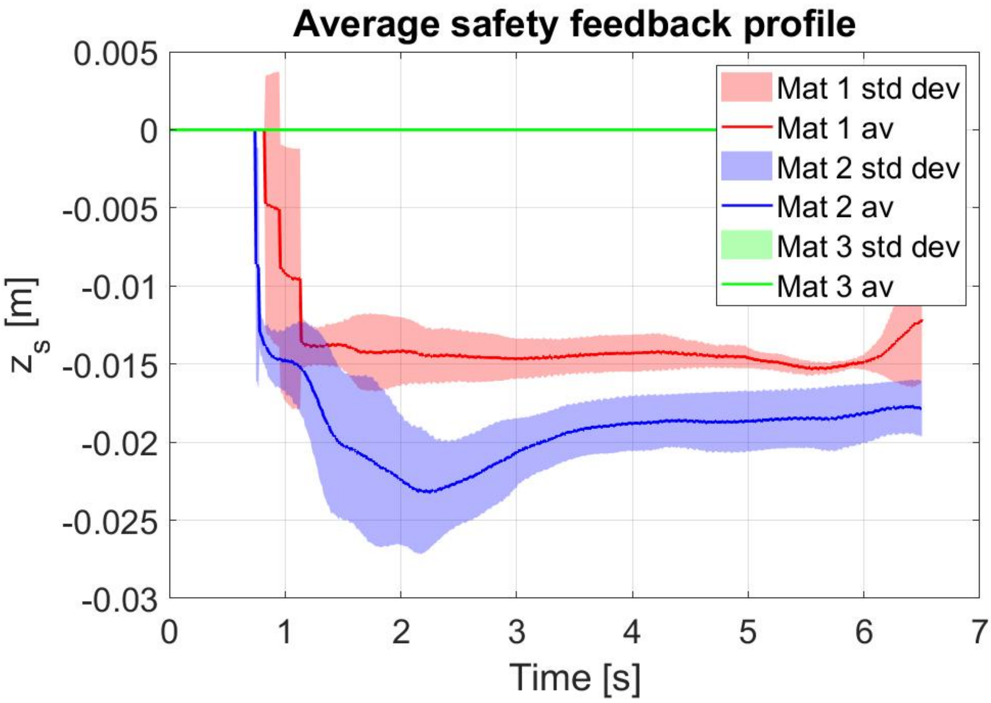

Figure 4.10: Safety position correction profile $\boldsymbol{z_s}$ for all materials

For the qualitative analysis, the answers to the questionnaire described in Chapter 3 were analyzed. In Figure 4.11, the results of the questionnaire are reported. The statistical analysis showed that, for statements S1, S2, S3, S4, S8, the results were non significant, with a p-value > 0.05. This corresponded to the expected outcome, and demonstrated that the proposed control strategy is similar to a constant impedance strategy in terms of usability, absence of inconsistency and mental workload. Looking at statement S5, S6 and S7, the results were significant, with a p-value < 0.05. In particular, regarding S5, the users found the materials easier to damage with Mode 1. Moreover, it was easier in Mode 1 for the user to distinguish the materials, even without visual feedback (S6). This means that the strategy simulate in an appropriate way a rigid behavior when contact was made with a soft material. Finally, S7 suggests that the strategy successfully prevents movement along the z-axis when needed, as users felt the inability to complete the assigned task.

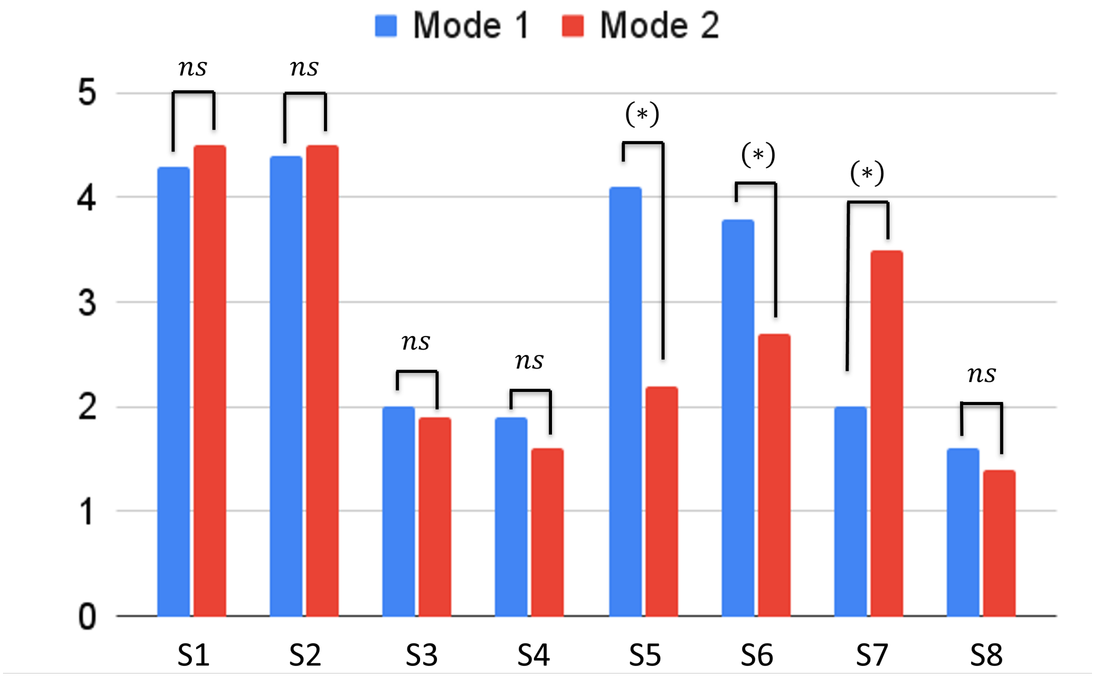

Figure 4.11: Questionnaire results

5 | Conclusions and future developments

In this study, an adaptive impedance controller was developed to assist the surgeon in vertebral osteotomy procedures. In this operation, the surgeon must avoid damaging the critical structures in the proximity of the vertebra, such as the spinal cord and blood vessels. The goal of the study was to change the stiffness of the robot, based on the contact force between the robot tooltip and the environment and on the human estimated force, obtained from the EMG signals of the user's arm. Moreover, a safety position command was generated when contact was made with delicate materials. Results showed that the proposed strategy successfully increases the stiffness of the robot when contact is made with delicate materials without causing end effector oscillations, and reduces the risk of damaging such materials, in terms of end effector contact force and displacement, compared to a constant impedance control strategy. The main limitation of this study is the applicability in a real scenario since the analysis should be performed with a robot equipped with a real surgical instrument. The force sensor is subjected to measurement noise, which increases in time due to internal overheating. This problem should be assessed since vertebral osteotomies are surgical operations that require several hours. The human force estimate obtained from the EMG signals was not satisfying enough. To improve the quality of the collected dataset, it would be interesting to substitute the MyoWristband with electrodes, placed on the shoulder and chest areas. Finally, the different sponges used in the experiments did not simulate accurately enough the properties of the spinal cord and blood vessels. For this reason, a more realistic experimental setup should be considered for future experiments.

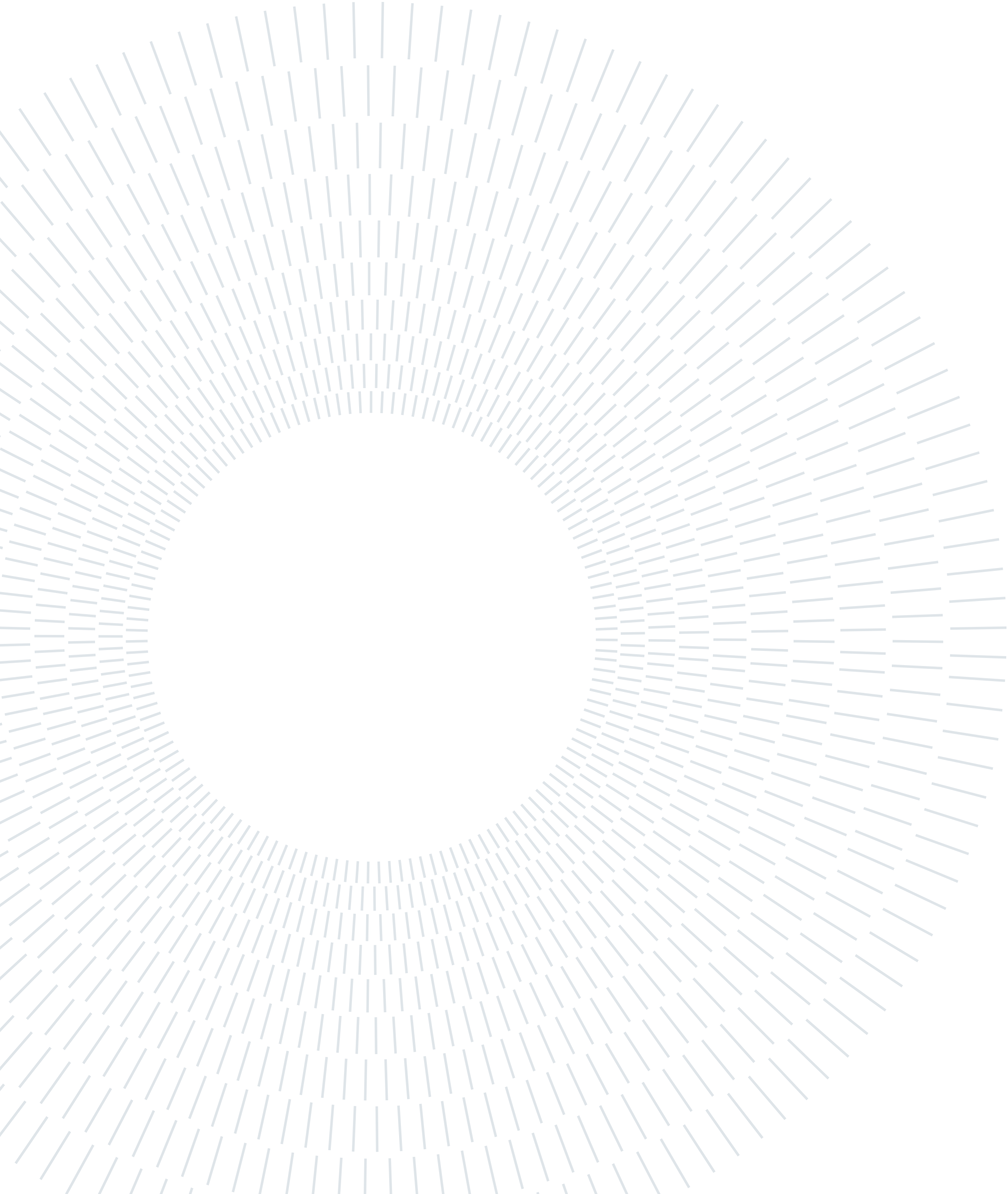

Bibliography

[1] Bryant JH Menger RP, Davis DD. Spinal osteotomy, 2022.

[2] Oussama Khatib Bruno Siciliano. *Springer Handbook of Robotics*. Springer-Verlag Berlin Heidelberg, 2008.

[3] S. Harrison Farber, Mark A. Pacult, Jakub Godzik, Corey T. Walker, Jay D. Turner, Randall W. Porter, and Juan S. Uribe. Robotics in spine surgery: A technical overview and review of key concepts. *Frontiers in Surgery*, 8, 2021.

[4] Swanand S Pathak Sakshi Bramhe. Robotic surgery: A narrative review. *Cureus Journal of Medical Science*, pages 1–7, 2022.

[5] Michael Stoffel Andreas Reinke Michael Behr Bernhard Meyer Carsten Stüer, Florian Ringel. Robotic technology in spine surgery: current applications and future developments. *PubMed*, pages 1–5, 2010.

[6] Patricia Freeman Jamie Henry Meghan Baldwin Clare K Fitzpatrick David Van-Sickle, Victoria Volk. Electrode placement accuracy in robot-assisted asleep deep brain stimulation. *Annals of Biomedical ENgineering*, 47:1212–1222, 2019.

[7] Maryam N. Shahin David J. Mazur-Hart, Nasser K. Yaghi and Ahmed M. Raslan. Stealth autoguide for robotic-assisted laser ablation for lesional epilepsy: illustrative case. *Journal of Neurosurgery*, pages 1–5, 2022.

[8] Jian Zhang, Weishi Li, Lei Hu, Yu Zhao, and Tianmiao Wang. A robotic system for spine surgery positioning and pedicle screw placement. *The International Journal of Medical Robotics and Computer Assisted Surgery*, 17(4):e2262.

[9] Azad-T.D. Cottrill E. et al Jiang, B. New spinal robotic technologies. *Front. Med*, 2019.

[10] Alexander D. Smith BS Annabelle Shaffer MS David T. Krist PhD Anant Naik, BS. Evaluating robotic pedicle screw placement against conventional modalities: a systematic review and network meta-analysis. *Neurosurgical Focus*, 2022.

[11] Shea Hesselbacher Isador H. Lieberman, Isador H. Lieberman. Robotic-assisted pedicle screw placement during spine surgery. *JBJS Essential Surgical Techniques*, pages 1–15, 2020.

[12] Meng Huang, Tyler Tetreault, Avani Vaishnav, Philip York, and Blake Staub. The current state of navigation in robotic spine surgery. *Annals of Translational Medicine*, 9:86–86, 01 2021.

[13] Ali Torabi Vivian K. Mushahwar Mahdi Tavakoli Mojtaba Sharifi, Javad K. Mehr. Impedance variation and learning strategies in human–robot interaction. *IEEE transaction on cybernetics*, pages 1–14, 2021.

[14] Lifang Xiao, Tangwen Yang, Benyan Huo, Xingang Zhao, Jianda Han, and Weiliang Xu. Impedance control of a robot needle with a fiber optic force sensor. In *2016 IEEE 13th International Conference on Signal Processing (ICSP)*, pages 1379–1383, 2016.

[15] Elisa Beretta, Elena De Momi, Ferdinando Rodriguez y Baena, and Giancarlo Ferrigno. Adaptive hands-on control for reaching and targeting tasks in surgery. *International Journal of Advanced Robotic Systems*, 12(5):50, 2015.

[16] H.-P. Huang and S.-S. ehen. Compliant motion control of robots by using variable impedance. *The International Journal of Advanced Manufacturing Technology*, pages 1–11, 1992.

[17] Hsieh-Yu Li, Theshani Nuradha, Sebaratnam Alex Xavier, and U-Xuan Tan. Towards a compliant and accurate cooperative micromanipulator using variable admittance control. In *2018 3rd International Conference on Advanced Robotics and Mechatronics (ICARM)*, pages 230–235, 2018.

[18] Zoe Doulgeri Theodora Kastritsi. A controller to impose a rcm for hands-on robotic-assisted minimally invasive surgery. *IEEE Transactions on medical robotics and bionics*, 3:392–401, 2021.

[19] Bernard Bayle Maciej Bednarczyk, Hassan Omran. Emg-based variable impedance control with passivity guarantees for collaborative robotics. *IEEE Robotics and automation letters*, 7:4307–4312, 2022.

[20] Bernard Bayle Maciej Bednarczyk, Hassan Omran. Passivity filter for variable impedance control. *IEEE/RSJ International Conference on Intelligent Robots and Systems (IROS)*, pages 1–6, 2020.

[21] Teng Li, Armin Badre, Hamid D. Taghirad, and Mahdi Tavakoli. Integrating

impedance control and nonlinear disturbance observer for robot-assisted arthroscope control in elbow arthroscopic surgery. In *2022 IEEE/RSJ International Conference on Intelligent Robots and Systems (IROS)*, pages 11172–11179, 2022.

[22] Joshua G. Petersen and Ferdinando Rodriguez Baena. A dynamic active constraints approach for hands-on robotic surgery. In *2013 IEEE/RSJ International Conference on Intelligent Robots and Systems*, pages 1966–1971, 2013.

[23] Dongsheng Xie Xingguang Duan Xi Fu Huanyu Tian, Zhe Han and Feng Niu. The region-based virtual fixtures control for invasive avoidance in hands-on robot-assisted mandibular angle split osteotomy. *12th IEEE International Conference on CYBER Technology in Automation, Control and Intelligent Systems*, pages 1–6, 2022.

[24] Minas V. Liarokapis, Panagiotis K. Artemiadis, Pantelis T. Katsiaris, Kostas J. Kyriakopoulos, and Elias S. Manolakos. Learning human reach-to-grasp strategies: Towards emg-based control of robotic arm-hand systems. In *2012 IEEE International Conference on Robotics and Automation*, pages 2287–2292, 2012.

[25] Duc Nguyen Quang, Pham Thien, and Tho Quan. Design, implementation and evaluation for a high precision prosthetic hand using myoband and random forest algorithm. 08 2019.

[26] At Hof. Emg and muscle force: An introduction. *Human Movement Science - HUM MOVEMENT SCI*, 3:119–153, 03 1984.

[27] Mehdi Shirzadi, Hamid Reza Marateb, Mónica Rojas-Martínez, Marjan Mansourian, Alberto Botter, Fabio Vieira dos Anjos, Taian Martins Vieira, and Miguel Angel Mañanas. A real-time and convex model for the estimation of muscle force from surface electromyographic signals in the upper and lower limbs. *Frontiers in Physiology*, 14, 2023.

[28] Hang Su, Wen Qi, Zhijun Li, Ziyang Chen, Giancarlo Ferrigno, and Elena De Momi. Deep neural network approach in emg-based force estimation for human–robot interaction. *IEEE Transactions on Artificial Intelligence*, 2(5):404–412, 2021.

[29] Shaoyang Hua, Congqing Wang, and Xuewei Wu. A novel semg-based force estimation method using deep-learning algorithm. *Complex Intelligent Systems*, 8:1–13, 04 2021.

[30] Jiaqi Xue and King Wai Chiu Lai. Dynamic gripping force estimation and reconstruction in emg-based human-machine interaction. *Biomedical Signal Processing and Control*, 80:104216, 2023.

[31] Fabio Galbusera and Tito Bassani. The spine: A strong, stable, and flexible structure with biomimetics potential. *Biomimetics (Basel, Switzerland).*

[32] Ki-Tack et al Kim. Osteotomy of the spine to correct the spinal deformity. *Asian spine journal*, 3(2):113–23, 2009.

[33] Kamil Cagri Kose, Omer Bozduman, Ali Erkan Yenigul, and Servet Igrek. Spinal osteotomies: indications, limits and pitfalls. *EFORT Open Reviews*, 2(3):73 – 82, 2017.

[34] Turner CH. Rho JY, Ashman RB. Young's modulus of trabecular and cortical bone material: ultrasonic and microtensile measurements. *Journal of Biomechanic*, 26(2):111–9, 1993.

[35] Ali P. Ebrahimi. Mechanical properties of normal and diseased cerebrovascular system. *Journal of vascular and interventional neurology*, 2(2):155–62, 2009.

[36] Peter Lambert. Dynamic characterization of kuka light-weight robot manipulators. Technical report, Center for Robotics Intelligent Machines Georgia Institute of Technology, 801 Atlantic Drive NW Atlanta, GA 30332, USA, 2012.

[37] G. Hirzinger, A. Albu-Schaffer, M. Hahnle, I. Schaefer, and N. Sporer. On a new generation of torque controlled light-weight robots. In *Proceedings 2001 ICRA. IEEE International Conference on Robotics and Automation (Cat. No.01CH37164)*, volume 4, pages 3356–3363 vol.4, 2001.

[38] Svemir Popić and Branko Miloradovic. Light weight robot arms-an overview. 03 2015.

[39] Stefano Chiaverini, Giuseppe Oriolo, and Ian D. Walker. *Kinematically Redundant Manipulators*, pages 245–268. Springer Berlin Heidelberg, Berlin, Heidelberg, 2008.

[40] Andreas Stemmer Günter Schreiber and Rainer Bischoff. The fast research interface for the kuka lightweight robot. *Innovative Robot Control Architectures for Demanding (Research) Applications (ICRA Workshop)*, 2010.

[41] KUKA Roboter GmbH. *KUKA.FastResearchInterface 1.0.* 2011.

[42] Darren M. Dawson Bin Xian Aman Behal, Warren Dixon. *Lyapunov-Based Control of Robotic Systems.* CRC Press, 2019.

[43] Darren M. Dawson. *Nonlinear Control of Electric Machinery.* CRC Press, 2019.

[44] C.N. Riviere, J. Gangloff, and M. De Mathelin. Robotic compensation of biological motion to enhance surgical accuracy. *Proceedings of the IEEE*, 94(9):1705–1716, 2006.

List of Figures

1 Examples of spinal deformities. Kyphosis: excessive curvature in the upper spine section. Lordosis: excessive curvature in the lower spine section . . . 1
2 On the left, a surgeon is depicted while using a small hammer and an osteotome (or chisel). In the middle, different types of osteotome are shown. On the right, a surgeon is holding a bone drill. 2

1.1 Pedicle screw operation outcome: screws are placed inside a vertebra to stabilize the spine. Left: front view. Right: side view. 5
1.2 Mazor X stealth edition platform. Navigation tracking camera (left), the base station (middle), bed-mounted robotic arm with end effector (right)[12] 6
1.3 Examples of EMG usage in modern medicine. Electrodes are placed on patients' muscles to measure their activity. Patients are asked to contract or tighten the involved muscles, i.e. closing the hand or bending the leg. . 9
1.4 Artificial neural networks can be used to estimate muscle forces from EMG measurements 10

2.1 High level description of vertebral bones sections 13
2.2 Vertebra top view: spinal cord position 14
2.3 Example of the vertebral osteotomy. On the left, the side view of the spine is shown. In red, the area of the vertebra that needs to be cut is represented. On the Right, the improved spine curvature after the osteotomy procedure is shown. 15
2.4 Example of a stress-strain curve 16

3.1 Picture of the KUKA LWR4+ at NEARLab 17
3.2 DH reference frames 19
3.3 Kuka Control Panel 23
3.4 FRI state machine with monitor and command mode 24
3.5 6 axis force/torque sensor, mounted on the KUKA 26

3.6 Representation of the calibration. In green, the reference frame of the seventh joint is shown. In red, the sensor frame of the force sensor is shown, rotated by an angle θ_r around the z-axis. 27
3.7 Scheme of the Multilayer Perceptron Regressor. Input: orientation of the end effector. Output: component x, y, z of the force sensor. 28
3.8 Scheme of the processing of the force signal: first an exponential smoothing filter is applied. Next, The sensor reference frame is aligned with the frame of the seventh joint. Then, the tool weight is compensated using a Multilayer Perceptron regressor. 29
3.9 MyoBand electromyography sensor 29
3.10 Scheme of the EMG signal processing. First, the muscle signals are sampled at 200 Hz. Then, a full wave rectification is applied and the signal envelope is extracted at 50 Hz. 30
3.11 EMG processed signals for the 8 channels of the forearm muscle activity. . 31
3.12 The configuration used in the data collection process 32
3.13 1DOF impedance model representation. k, d and m represent the robot stiffness, damping and inertia, respectively. F_{ee} is the force exherted from the robot end effector on the environment, while F_{ext} is the external force acting on the robot. 33
3.14 Schemes of Impedance (upper) and Admittance (lower) control logic. In Impedance control, given a position reference, the position error is changed into a force signal. Conversely, an admittance controller receives as input a force error and gives as output a position. 34
3.15 Conceptual scheme of the system: impedance parameters are adapted based on the EMG signals and the measured contact force between the robot and the environment. 36

3.16 Scheme of the adaptive impedance control law with safety position feedback: the Cartesian reference pose $\boldsymbol{x_{ref}}$ is obtained as the difference between the position imposed by the human $\boldsymbol{x_h}$ and the safety position feedback $\boldsymbol{x_s}$, generated by multiplying $\boldsymbol{F_{ee}}$ and the gain matrix $\boldsymbol{P}$. The position error $\tilde{\boldsymbol{x}}$ is then calculated by subtracting $\boldsymbol{x_{ref}}$ and the current Cartesian pose, $\boldsymbol{x_{curr}}$. This error is multiplied by a variable stiffness matrix $\boldsymbol{K}$, controlled by an adaptive law which receives the human estimated force, $\boldsymbol{F_h}$, derived from an EMG signal and the contact force measured by the force sensor, $\boldsymbol{F_{ee}}$, as inputs. $\boldsymbol{F_{ee}}$ is measured from the force $\boldsymbol{F_r}$ that the robot exherts on the environment. The current Cartesian velocity, $\dot{\boldsymbol{x}}_{\boldsymbol{curr}}$, is used to compute the damping term $\boldsymbol{D(D_n, \dot{x}_{curr})}$, where $\boldsymbol{D_n}$ is the normalized damping matrix. The torque command in the joint space $\boldsymbol{\tau_{cmd}}$ is generated by using the Jacobian pseudo-inverse $\boldsymbol{J_{pin}^{-1}}$ and summing the inertial term $\boldsymbol{f}_d(\boldsymbol{q}, \dot{\boldsymbol{q}}, \ddot{\boldsymbol{q}})$, $\boldsymbol{q}, \dot{\boldsymbol{q}}, \ddot{\boldsymbol{q}}$ are the vectors of robot joint position, velocity, and acceleration, respectively. 37
3.17 Scheme of the four possible contact conditions. 1a and 2a: contact happens with a material with a high Young's modulus. 1b, first phase of the contact. 2b, the material has a low Young's modulus. 39
3.18 Chosen materials: polyurethane sponges (upper left), foam rubber (down left), PVA sponge (upper right), PLA vertebra phantom (down right). . . 47
3.19 z_d is computed from the contact point $z_{contact}$ to the minimum z position that the tooltip reaches z_{min}. 48
3.20 Experimental setup in the User Study. The user guides the robot, equipped with the force sensor against different materials, placed inside a box. In Mode 2, the user is also wearing the MyoWristband on the forearm. 49
3.21 Experimental setup in the User Study: user perspective. 49

4.1 Validation of the force sensor tool weight compensation. In red, true force values are represented, while in blue the force predicted by the MLP is shown. 53
4.2 Loss function of training and validation dataset 54
4.3 Human force estimated online with the LSTM trained model. Depending on the muscle activity of the user, the predicted force changes between high and low values. 55
4.4 Upper left: end effector z position, $\boldsymbol{z_{curr}}$. Upper right: contact force, $\boldsymbol{F_{ee_z}}$. Down left: robot stiffness, $\boldsymbol{k_z}$. Down right: position feedback, $\boldsymbol{z_s}$. Contact with polyurethane. 56

4.5 Validation experiments: comparison of the boxplots of the stiffness $\boldsymbol{k_z}$ for all the materials 57
4.6 Validation experiments: comparison of the boxplots of the safety position correction $\boldsymbol{z_s}$ for all the materials 57
4.7 Boxplots of the mean force $\hat{F}_{ee_z}$ for each material 59
4.8 Boxplots of the mean displacement $\hat{z}_s$ for each material 59
4.9 Stiffness profile $\boldsymbol{k_z}$ for all materials 60
4.10 Safety position correction profile $\boldsymbol{z_s}$ for all materials 61
4.11 Questionnaire results 62

List of Tables

3.1 DH parameters 19
3.2 Joint limits 22
3.3 For both tasks, users were asked to express their level of agreement with each of the 8 statements reported 50
3.4 Values of the parameters selected for the control strategy 51

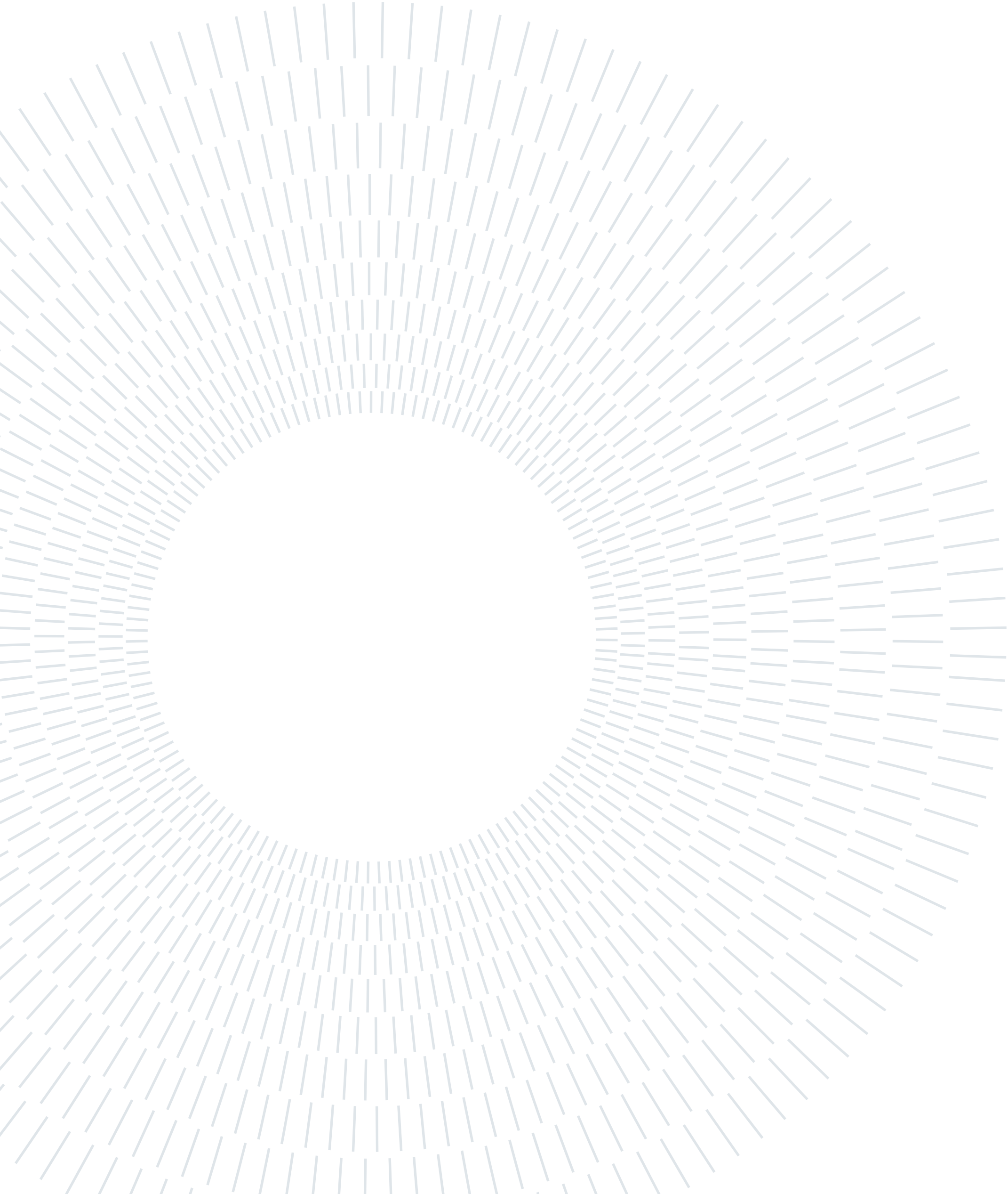

Acknowledgements

Vorrei ringraziare per prima cosa la professoressa Elena De Momi e tutti i membri del NEARLab, dottorandi e tesisti, con un riguardo speciale verso Elisa, senza la quale non sarei mai riuscito a laurearmi, e verso Junling, che mi ha aiutato innumerevoli volte.

Un grazie speciale ad Albi, Sara, Massi, Flavia, Peco, LaFra, Ginni, Dani, Petru, Co, Diego, Mike, Ele, Dave e tutta la squadra A.S.Intomatici.

Un grazie speciale ai CCini Bando, Bensa, Dipe, Simmi, Goli, Pol, Gazzo, Giablu, Filo, Moss, Cri, Luca, Brina, Gabbo, Merell, Ali, Bianca, Gulli, Mecha, il Man e Otti CCina onoraria.

Un grazie speciale a Tobi, Cathy, Ila, Gianlu e all'appartamento di via Ingegnoli.

Un grazie speciale a Luca e alle pause estive in valle Aurina.

Infine un grazie specialissimo a tutta la mia famiglia: ai miei genitori Thema e Thefa, a mia sorella, alla mia nonna, alla micia, a Teofilatto e Hunter.

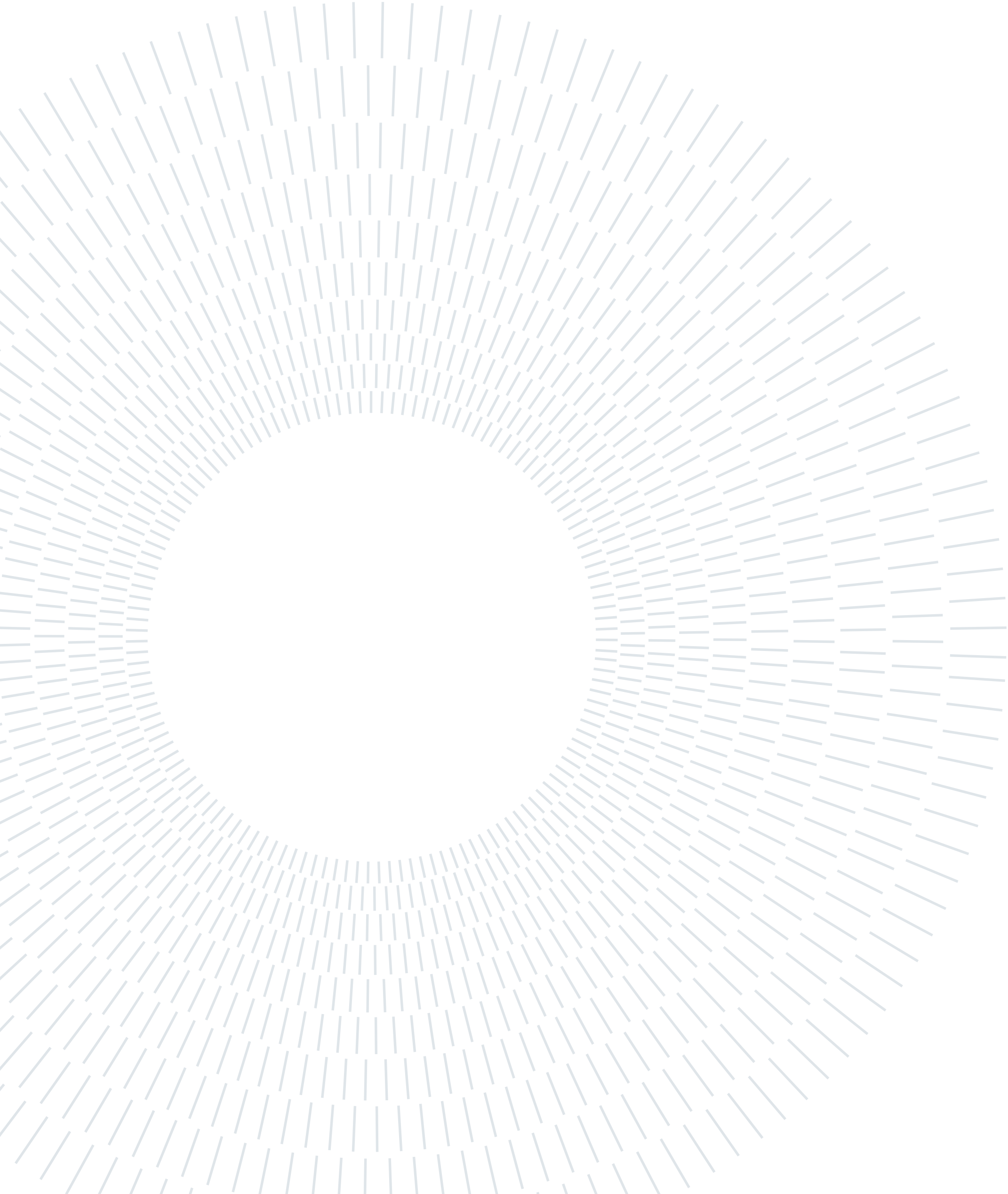Grazie di cuore.